Wave-Based Flutter Analysis of Flexible Wings with Anechoic Stub Damping

Benjamin Chouvion[a,*]

[a] CREA, École de l'air et de l'espace, F-13660 Salon-de-Provence, France

---

Abstract

This research investigates a wave-based framework for analyzing and controlling aeroelastic flutter in flexible, high-aspect-ratio aircraft wings. Unlike traditional modal-based approaches that rely on spatial discretization, this method uses exact wave propagation equations to describe the structural dynamics of bending and torsion. The study introduces an anechoic stub as a passive damping device, which aims to absorb vibrational energy and mitigate instabilities across a broad frequency range. Numerical simulations apply this framework to benchmark models like the Goland and HALE wings, comparing the effectiveness of the anechoic stub against classical tuned mass dampers. The results demonstrate that strategic spatial placement of these damping mechanisms can significantly postpone the onset of flutter, offering a robust alternative for enhancing aircraft stability.

Keywords: anechoic stub, flutter control, wave reflection, vibration control, wave damping, Goland wing, HALE wing, tuned-mass-damper

---

1. Introduction

High-Altitude Long-Endurance (HALE) aircraft rely on extremely slender wings with very high aspect ratios, enabling efficient long-duration flight but inducing pronounced aeroelastic effects. In such configurations, structural flexibility plays a dominant role, leading to strong coupling between aerodynamic forces and structural deformations [1]. Among the resulting aeroelastic phenomena, flutter remains a critical design constraint, as it may limit the flight envelope or require additional structural reinforcement, thereby reducing performance. The aeroelastic analysis of flexible wings has traditionally been conducted using modal-based approaches, where the structural response is expressed as a superposition of vibration modes coupled with aerodynamic models ranging from quasi-steady to fully unsteady formulations. Foundational contributions [2, 3] established the theoretical framework for such analyses, which has since been widely applied to rigid wings or HALE configurations. These methods have proven effective for predicting flutter and divergence in benchmark cases such as the Goland wing [4] or an HALE-representative wing [5]. These approaches rely on an approximated spatially discretized representation of the structure, often made by finite element approximation or a discrete number of Rayleigh-Ritz continuous functions. An alternative description consists in formulating

---

[*] Corresponding author

Email address: `benjamin.chouvion@ecole-air.fr` (Benjamin Chouvion) the structural dynamics in terms of propagating waves. Wave-based approaches provide an exact representation of the response of slender structures and naturally account for reflection and transmission phenomena [6–8]. Their theoretical basis can be traced back to classical wave propagation theory in beams [9, 10]. More recently, exact formulations of aeroelastic systems have been proposed by Liska and Dowell [11], highlighting the advantages of non-modal approaches. Despite these advances, the application of wave-based methods to flutter analysis of finite wings remains limited.

Flutter prediction is classically performed by solving a parameter-dependent eigenvalue problem and tracking the evolution of eigenvalues with increasing flow velocity. While widely used, this approach may become cumbersome when dealing with complex or highly coupled systems. An alternative strategy introduced by Balaji and Leamy [12, 13] has been especially developed for exact wave-based formulation and is based on the residue of a perturbed eigenproblem. Using an exact continous approach, such as the wave-based formulation, the governing equation of motion to solve reduced to a nonlinear eigenvalue problem with an infinite number of solutions [14, 15]. This formulation requires a robust framework for stability assessment and has remained largely unexplored in aeroelastic flutter problems.

In parallel, flutter mitigation strategies have traditionally relied on structural damping, active control [16], or tuned devices such as tuned mass dampers [17, 18]. These solutions are often limited by their narrowband efficiency or by implementation constraints in lightweight structures. Wave-based damping concepts offer an alternative perspective by targeting the propagation mechanisms responsible for resonance build-up. In particular, anechoic terminations or stubs aim at absorbing incident waves and minimizing reflections. Initially developed for acoustic wave attenuation [19], there are also some studies for structural vibration waves [20]. Unlike tuned devices, such concepts can operate over a broad frequency range and can be designed to interact selectively with specific wave components. Although related to acoustic black hole concepts [21, 22], anechoic stubs rely on different physical mechanisms and are more readily adaptable to structural applications. Such damping mechanisms are typically employed to reduce the vibrational energy of forced systems at resonance. However, to the author's knowledge, no study has yet explored the use of an anechoic termination as a means of controlling aeroelastic effects.

Motivated by these observations, the present work proposes a wave-based framework for the flutter analysis of finite wings and investigates a passive damping strategy based on an anechoic stub. The structural dynamics are modelled using propagating waves, leading to an exact formulation that does not rely on modal truncation. Aeroelastic stability is assessed using the perturbed eigenproblem residue approach, providing an alternative to classical eigenvalue tracking methods. The proposed framework is applied to several benchmark configurations, including the Goland wing and representative HALE wings, and is shown to accurately predict flutter and divergence speeds for different aerodynamic models, ranging from quasi-steady to unsteady formulations. A general anechoic stub is also introduced as a passive damping device for flutter mitigation. Unlike tuned mass dampers or classical structural damping, this approach is not frequency-tuned and acts directly on wave propagation, enabling broadband attenuation and efficient control of the instability through appropriate spatial placement.

The remaining of the paper is organized as follows. The wave-based approach modelling of the wing and the aerodynamic model are detailed in Section 2. Section 3 presents how the added absorber, tuned mass damper or anechoic termination, can be efficiently accounted for in the wave-based framework. Finally, comparison parametric studies on the absorber designs are given in Section 4.

2. Aeroelastic simulation with a wave-based approach

2.1. Wing modelling under unsteady flow

Consider a uniform, straight wing with constant cross-section, modelled as a clamped-free linear beam undergoing both in-plane bending and torsion. Although detailed equations of motion of such system are given in different textbooks, for instance in [2], the main steps of derivation are given next for completeness and introducing the notation. The latter is slightly different, the bending motion is for instance defined positive upwards, and follows the one used in [23], simplified to a two-dimensional case with bending and torsion only. The model is illustrated in Fig. 1.

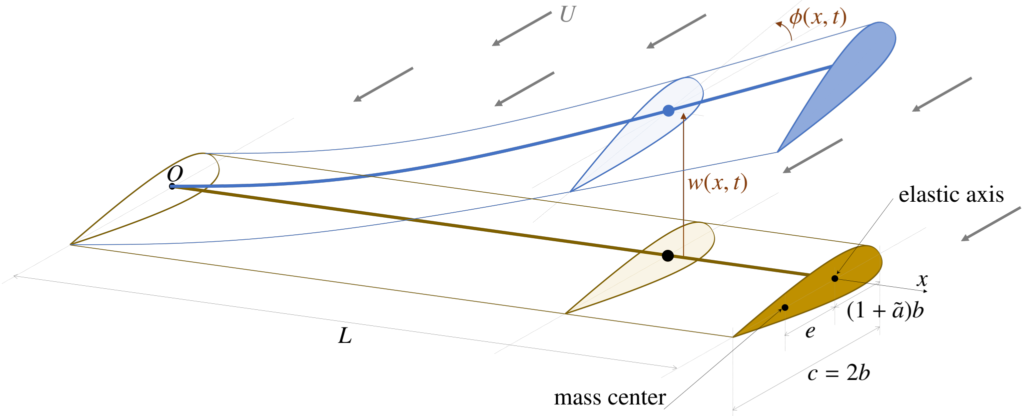

Figure 1: Wing modelled as a linear beam with kinematics in bending and torsion. The definition of the geometric parameters notation is given in Table 1.

Assuming small out-of-plane motion of the wing, characterized by the transverse displacement w, and rotation of the cross-section ϕ, both function of the span-wise coordinate x time t, the kinetic and potential energies are given -respectively- as follows:

$$\mathcal{T} = \frac{1}{2}\int_0^L (m\dot{w}^2 + I_P\dot{\phi}^2 - 2me\dot{\phi}\dot{w})\,\mathrm{d}x \tag{1}$$

$$\mathcal{U} = \frac{1}{2}\int_0^L (GJ\phi'^2 + EIw''^2)\,\mathrm{d}x \tag{2}$$

The definition of all the geometric, material and stiffness parameters of the wing are given in Table 1. An important one is the distance e between the elastic and mass centers of the cross section along the chordwise direction. It characterises the static unbalance and is defined positive when the center of mass is toward the trailing edge from the elastic axis (as depicted in Fig. 1). The notation $\dot{(\cdot)}$ and $(\cdot)'$ are used for time and space derivative respectively.

The -linearized- virtual work done by aerodynamic forces is:

$$\delta W_a = \int_0^L (F_w\delta w + M_\phi\delta\phi)\,\mathrm{d}x \tag{3}$$

The lift force F_w and moment M_ϕ are defined following a strip-theory, i.e. there are no aerodynamic coupling spanwise. They follow Theodorsen theory – unsteady aerodynamics for a thin

Table 1: Geometrical and physical parameters of the Goland wing and an HALE-type wing (numerical values from [24]).

Parameter	Notation	Value	
		Goland wing	HALE wing
Chordwise position of the elastic axis with respect to mid-chord (dimensionless)	$\tilde{a}$	-0.34	0
Semi-chord ($= c/2$) (m)	b	0.9144	0.5
Chord (m)	c	1.8288	1
Offset of the mass centroid from the elastic axis (m)	e	$0.1c$	0
Spanwise bending rigidity ($\mathrm{N\,m^2}$)	EI	9.77×10^6	2×10^4
Torsional rigidity ($\mathrm{N\,m^2}$)	GJ	0.987×10^6	1×10^4
Cross-sectional mass polar moment of inertia (kg m)	I_p	8.64	0.1
Half span - beam length (m)	L	6.096	16
Mass per unit span ($\mathrm{kg\,m^{-1}}$)	m	35.71	0.75
Air density ($\mathrm{kg\,m^{-3}}$)	ρ	1.225	0.0889

airfoil assuming simple harmonic motion [2]:

$$F_w = 2\pi\rho U b C(\omega_r)\left[-\dot{w} + U\phi + b\left(\frac{1}{2} - \tilde{a}\right)\dot{\phi}\right] + \pi\rho b^2\left(-\ddot{w} + U\dot{\phi} - b\tilde{a}\ddot{\phi}\right) \tag{4a}$$

$$M_\phi = b\left(\frac{1}{2} + \tilde{a}\right)F_w - \pi\rho b^3\left[-\frac{1}{2}\ddot{w} + U\dot{\phi} + b\left(\frac{1}{8} - \frac{\tilde{a}}{2}\right)\ddot{\phi}\right] \tag{4b}$$

In these expression, U denotes the airspeed and $C(\omega_r)$ is the Theodorsen's circulation function of the reduced frequency ω_r. The reader can refer to Table 1 for the definition of the other parameters. In some numerical applications presented in Section 2.4, an aerodynamic model with quasi-steady assumptions ($C(\omega_r) = 1$) will also be used for validation. In a more general situation, and especially for the Goland wing from which some clear differences have been found on flutter speed depending on the aerodynamic model [5, 25], this assumption is not appropriate and one must use the exact definition of the complex-value function $C(\omega_r)$ given by:

$$C(\omega_r) = \frac{H_1^{(2)}(\omega_r)}{H_1^{(2)}(\omega_r) + \mathrm{i}H_0^{(2)}(\omega_r)} \tag{5}$$

where $H_n^{(2)}(\omega_r)$ are Hankel functions which can be expressed in terms of Bessel functions of the first kind and second kind, noted respectively J_n and Y_n:

$$H_n^{(2)}(\omega_r) = J_n(\omega_r) - \mathrm{i}Y_n(\omega_r). \tag{6}$$

Equations or motion are obtained by setting the first variation of action equal to zero, i.e.:

$$\int_0^t \delta\mathcal{L}\,\mathrm{d}t = \int_0^t \left(\delta\left(\mathcal{T} - \mathcal{U}\right) - \delta W_a\right)\mathrm{d}t = 0 \tag{7}$$

The Lagrangian $\mathcal{L}$ is expressed as the integral of a space-dependent function, in other words: $\mathcal{L} = \int_0^L \widehat{\mathcal{L}}\,\mathrm{d}x$. Thus, integration by parts is possible and leads to an expression of Eq. (7) only in terms of δw and $\delta\phi$. Equating each variation to zero gives the two governing equations of motion:

$$I_P\ddot{\phi} - me\ddot{w} - GJ\phi'' - M_\phi = 0 \tag{8a}$$

$$m\ddot{w} - me\ddot{\phi} + EIw'''' - F_w = 0 \tag{8b}$$

In these equations, pitch and plunge motions are coupled by both the aerodynamic forces and inertia coupling (due to the offset e).

For the remaining of the paper, one will use a adimensional version of these equations. For this matter, let introduce the dimensionless variables (denoted in Greek letters):

$$\tau = \frac{t}{T}, \quad \chi = \frac{x}{L}, \quad \upsilon = \frac{w}{L},$$

with the characteristic time

$$T = L^2\sqrt{\frac{m}{EI}},$$

the dimensionless parameters (denoted either with a tilde or in Greek letters)

$$\tilde{e} = \frac{e}{L}, \quad \tilde{b} = \frac{b}{L}, \quad \beta = \frac{I_P}{mL^2}, \quad \gamma = \frac{GJ}{EI}, \quad \mu = \frac{\rho b L}{m},$$

and the reduced airspeed

$$\Upsilon = \frac{UT}{L}.$$

With these definitions, the governing equations of motion become:

$$\beta\ddot{\phi} - \tilde{e}\ddot{\upsilon} - \gamma\phi'' - \tilde{M}_\phi = 0 \tag{9a}$$

$$\ddot{\upsilon} - \tilde{e}\ddot{\phi} + \upsilon'''' - \tilde{F}_\upsilon = 0 \tag{9b}$$

with the dimensionless aerodynamic forces

$$\tilde{F}_\upsilon = 2\pi\mu\Upsilon C(\omega_r)\left[-\dot{\upsilon} + \Upsilon\phi + \tilde{b}\left(\frac{1}{2} - \tilde{a}\right)\dot{\phi}\right] + \pi\mu\tilde{b}\left(-\ddot{\upsilon} + \Upsilon\dot{\phi} - \tilde{b}\tilde{a}\ddot{\phi}\right) \tag{10a}$$

$$\tilde{M}_\phi = \tilde{b}\left(\frac{1}{2} + \tilde{a}\right)F_\upsilon - \pi\mu\tilde{b}^2\left[-\frac{1}{2}\ddot{\upsilon} + \Upsilon\dot{\phi} + \tilde{b}\left(\frac{1}{8} - \frac{\tilde{a}}{2}\right)\ddot{\phi}\right] \tag{10b}$$

In these last expressions and for the remaining of the paper (Eq. (9) onwards), the derivative $(\dot{\cdot})$ and $(\cdot)'$ refer to partial differentiation with respect to the dimensionless time τ and space χ variables, respectively.

2.2. *Wave-based solution*

The objective of this section is not to simulate the time response solution of Eq. (9) but solely to determine the critical flutter speed. The originality of the proposed wave-based approach is to use neither time integration or spatial discretization (Rayleigh-Ritz function, mode shapes, finite elements, etc.) for this matter. Instead, one is going to use a wave-based solution and the ’perturbed eigen problem residue approach’ mentioned in [13]. A similar *exact* approach for flutter speed prediction – the term exact relates to the fact that the solution is not approximated by any spatial discretization, was used in [26] but with simplified aerodynamics.

2.2.1. *Wave description*

Let note $\boldsymbol{u}$ the vector that contains the kinematics variables $\boldsymbol{u} = \begin{bmatrix}\phi & \upsilon\end{bmatrix}^{\mathrm{T}}$, and consider a small dynamical perturbation $\delta\boldsymbol{u} = \begin{bmatrix}\delta\phi & \delta\upsilon\end{bmatrix}^{\mathrm{T}}$ around the equilibrium state $\boldsymbol{u}_{\mathrm{eq}} = (0, 0)$. Substituting the expression $\boldsymbol{u} = \boldsymbol{u}_{\mathrm{eq}} + \delta\boldsymbol{u}$ in Eq. (9) gives an identical set of equation, except that the dynamical variables now represent small perturbations. For simplification, the notation $(\phi, \upsilon, \boldsymbol{u})$ is kept, bearing in mind these actually characterize small perturbation dynamics. The linear homogeneous partial differential equations (9) admit an harmonic wave-based solution, whose frequency is complex-valued and unknown[1]. Let then look for a general wave form of the assumed periodic kinematics (more exactly pseudo-periodic as the frequency is complex-valued), solution of Eq. (9), such that:

$$\boldsymbol{u}(\chi, \tau) = \hat{\boldsymbol{u}}\mathrm{e}^{\kappa\chi}\mathrm{e}^{\lambda\tau} + \mathrm{c.c.} \tag{11}$$

The $\hat{(\cdot)}$ notation relates to wave amplitude. c.c denotes the complex conjugate. The complex frequency λ is generally composed of a real part, describing damping over time, and an imaginary part that corresponds to the (real) dimensionless frequency of the oscillating response. κ is a generic dimensionless complex wavenumber coupled to the dimensionless complex frequency λ via the dispersion relation obtained by substituting back the form (11) into (9) and solving for arbitrary τ and χ. Doing so, the obtained set of equations can be written under the following matrix form:

$$\boldsymbol{D}(\kappa, \lambda, \Upsilon)\begin{bmatrix}\hat{\phi}\\ \hat{\upsilon}\end{bmatrix} = \boldsymbol{0}. \tag{12}$$

The detailed expression of $\boldsymbol{D}(\kappa, \lambda, \Upsilon)$ is given in Appendix A for both the current unsteady aerodynamic model and a simplified version of such.

Equation (12) has non-trivial solution if and only if the determinant of $\boldsymbol{D}$ is equal to 0. Solving for $\det(\boldsymbol{D}(\kappa, \lambda, \Upsilon)) = 0$ gives the dispersion relation from which the relationship between κ and λ is obtained. The dispersion relation is a cubic polynomial in κ^2 and has 6 complex roots $\pm\kappa_i(\lambda)$ $(i = 1,\ 2,\ 3)$[2]. Their full expression is not given for brevity but it can be readily derived with the aid of symbolic computation software. The general motion solution of the governing equation (9) is therefore the sum of 6 waves whose each wavenumber is one of the complex roots. In order to simplify the analytical wave-based expressions and the associated numerical implementation, one choses to identify, and organise, the wavenumbers associated with positive χ-direction of travel among the six complex roots.

For this matter, the amplitude growth/decay of waves or even the notion of energy transport that could be used to characterize the direction of travel of the different waves cannot here be relied on due to the possible instability creating energy growing everywhere in the structure. Instead, the sign of phase velocity is analysed. Let consider a single wave, with a wavenumber κ_i solution of the dispersion relation, decomposed on its real and imaginary part to separate amplitude and phase:

$$\begin{aligned}\boldsymbol{u}(\chi, \tau) &= \hat{\boldsymbol{u}}\mathrm{e}^{\kappa_i\chi}\mathrm{e}^{\lambda\tau} + \mathrm{c.c}\\ &= \hat{\boldsymbol{u}}\,\mathrm{e}^{\mathrm{Re}(\kappa_i)\chi + \mathrm{Re}(\lambda)\tau}\mathrm{e}^{\mathrm{i}\left(\mathrm{Im}(\kappa_i)\chi + \mathrm{Im}(\lambda)\tau\right)} + \mathrm{c.c.}\end{aligned} \tag{13}$$

---

[1] This contrasts to forced vibration problems excited at a given excitation frequency (see for instance different examples in [27] for linear dynamics of space truss-like structure or [28] for beam-like structures with nonlinear joints).

[2] The dependency of κ_i in λ will be omitted in the rest of the paper, but bear in mind that its value can be calculated for any given complex-valued λ.

Knowing that a wave *travels* when a point of constant phase moves in space, the constant-phase point is searched for by differentiated the phase $(\operatorname{Im}(\kappa_i)\chi + \operatorname{Im}(\lambda)\tau)$ with respect to time. This gives the following definition of the phase velocity:

$$\frac{\mathrm{d}\chi}{\mathrm{d}\tau} = -\frac{\operatorname{Im}(\lambda)}{\operatorname{Im}(\kappa_i)}. \tag{14}$$

The minus sign in the above equation appears due to the convention used in the time-dependency. In order to make the wave travels toward the positive χ-direction, the phase velocity must be positive. So, the three κ_i-values kept are the ones such that $-\operatorname{Im}(\lambda)/\operatorname{Im}(\kappa_i) > 0$[3]. When both $\tilde{e} = 0$ and $\Upsilon \to 0$, the equations of motion (9) simplifies to that of a simple continuous beam under uncoupled bending and torsional movements. The wavenumbers that tend, in these conditions, to those of purely propagating torsional wave, and purely propagating and decaying flexural waves, will be noted κ_1, κ_2 and κ_3, respectively.

In addition to providing the dispersion relation, Eq. (12) also defines the relationship between waves amplitudes associated with mainly bending motion and those of mainly torsional motion. For this matter, one simply needs to substitute a wavenumber solution κ_i within (12) and looking for the ratio $\hat{\upsilon}/\hat{\phi}$ or $\hat{\phi}/\hat{\upsilon}$. Following the above definition of the κ_i values, it is convenient to use the ratio that tend to 0 when there are no coupling, those are $\bar{X}_1 = \hat{\upsilon}(\kappa_1)/\hat{\phi}(\kappa_1)$, $X_2 = \hat{\phi}(\kappa_2)/\hat{\upsilon}(\kappa_2)$ and $X_3 = \hat{\phi}(\kappa_3)/\hat{\upsilon}(\kappa_3)$. Closed form expressions of $X_i(\kappa_i)$ can be found analytically from (12) and are detailed in Appendix A.

Overall, going back to the six coupled waves solution of the dispersion relation, and following the choice of wavenumbers explained above, the pitch and plunge movement of the wing can then be expressed as a sum of coupled waves travelling in the positive and negative χ-directions, such that:

$$\phi(\chi,\tau) = \sum_{i=1}^{3}\left(\hat{\phi}_i^{+}\mathrm{e}^{\kappa_i\chi} + \hat{\phi}_i^{-}\mathrm{e}^{-\kappa_i(\chi-1)}\right)\mathrm{e}^{\lambda\tau} + \text{c.c} \tag{15a}$$

$$\upsilon(\chi,\tau) = \sum_{i=1}^{3}\left(\hat{\upsilon}_i^{+}\mathrm{e}^{\kappa_i\chi} + \hat{\upsilon}_i^{-}\mathrm{e}^{-\kappa_i(\chi-1)}\right)\mathrm{e}^{\lambda\tau} + \text{c.c}, \tag{15b}$$

with the coupling coefficients defined as

$$\hat{\phi}_2^{\pm} = X_2\hat{\upsilon}_2^{\pm} \tag{16a}$$

$$\hat{\phi}_3^{\pm} = X_3\hat{\upsilon}_3^{\pm} \tag{16b}$$

$$\hat{\upsilon}_1^{\pm} = \bar{X}_1\hat{\phi}_1^{\pm}. \tag{16c}$$

In these expression, $\hat{\phi}_i^{+}$ and $\hat{\upsilon}_i^{+}$ are the complex amplitudes of the waves travelling in the positive χ-direction; while $\hat{\phi}_i^{-}$ and $\hat{\upsilon}_i^{-}$ are related to negative χ-direction propagation. They originate from the bounds of the beam-like wing, that is respectively in $\chi = 0$ and $\chi = 1$. Overall, there are only 6 unknown wave amplitudes required to characterize the coupled pitch and plunge movement,

---

[3] Because λ takes complex values, the waves are almost never purely decaying – i.e. $\operatorname{Im}(\kappa_i) = 0$ is an exception that does not appear often in the simulation. In case it does, for instance when there are neither bending/torsion coupling or damping, one makes sure to have the wave decays in the positive χ-direction by keeping the wavenumber such that $\operatorname{Re}(\kappa_i) < 0$

three travelling in the positive χ-direction and three in the negative χ-direction. They are function of the complex frequency λ, the airflow velocity Υ and the wing boundary conditions. In a more compact form, Eq. (15) can be rewritten as :

$$\begin{bmatrix}\phi\\ \upsilon\end{bmatrix}(\chi,\tau)=\begin{bmatrix}\boldsymbol{c}_\phi\\ \boldsymbol{c}_\upsilon\end{bmatrix}\begin{bmatrix}\mathrm{e}^{\boldsymbol{\kappa}\chi} & \mathrm{e}^{\boldsymbol{\kappa}(1-\chi)}\end{bmatrix}\begin{bmatrix}\hat{\boldsymbol{u}}^+\\ \hat{\boldsymbol{u}}^-\end{bmatrix}\mathrm{e}^{\lambda\tau}+\mathrm{c.c} \tag{17}$$

where

$$\boldsymbol{c}_\phi=\begin{bmatrix}1 & X_2 & X_3\end{bmatrix} \quad \text{and} \quad \boldsymbol{c}_\upsilon=\begin{bmatrix}\bar{X}_1 & 1 & 1\end{bmatrix}.$$

The unknown wave amplitudes form the components of vector $\hat{\boldsymbol{u}}^\pm$, such that $\hat{\boldsymbol{u}}^\pm=\begin{bmatrix}\hat{\phi}_1^\pm & \hat{\upsilon}_2^\pm & \hat{\upsilon}_3^\pm\end{bmatrix}^{\mathrm{T}}$, and $\boldsymbol{\kappa}$ is a $[3\times3]$-diagonal matrix whose components are the κ_i values retained.

Instead of a classical finite element discretization in which the degrees of freedom would represent nodal displacements, here the variable are the positive and negative ongoing wave amplitudes taken at each wing end. Expression (17) gives a wave-based description of the dynamics of an *infinite* wing under aerodynamic forces. In Ref. [7] a wave-based approach was used to study linear vibrations in *finite* Euler-Bernouilli beams. Here, the approach is similar with the exception that flexural and torsional waves are coupled (see Eq. (8)) from aerodynamics effects.

2.2.2. *Taking account of the boundary conditions*

In order to calculate the local reflection coefficient matrices at boundaries, one uses the most general way of finding local transmission coefficient matrix that relates reflected waves to incident waves by writing the equations that define the boundary in the following form [27]

$$\boldsymbol{C}\hat{\boldsymbol{u}}^{\mathrm{crea}}+\boldsymbol{H}\hat{\boldsymbol{u}}^{\mathrm{inc}}=\boldsymbol{0} \tag{18}$$

where $\hat{\boldsymbol{u}}^{\mathrm{crea}}$ and $\hat{\boldsymbol{u}}^{\mathrm{inc}}$ are the wave amplitudes created and impinging on the boundary respectively. The local reflection coefficient matrix $\boldsymbol{T}_{\mathrm{loc}}$ that relates created to impinging waves, defined such that $\hat{\boldsymbol{u}}^{\mathrm{crea}}=\boldsymbol{T}_{\mathrm{loc}}\hat{\boldsymbol{u}}^{\mathrm{inc}}$, is then found with $\boldsymbol{T}_{\mathrm{loc}}=-\boldsymbol{C}^{-1}\boldsymbol{H}$.

Using Eq. (17) in $\chi=0$ the three wing root boundary conditions (clamped) write, following the form given in (18):

$$\begin{matrix}\phi(0)=0 & \rightarrow\\ \upsilon(0)=0 & \rightarrow\\ \upsilon'(0)=0 & \rightarrow\end{matrix} \qquad \begin{bmatrix}\boldsymbol{c}_\phi\\ \boldsymbol{c}_\upsilon\\ \boldsymbol{c}_\upsilon\boldsymbol{\kappa}\end{bmatrix}\hat{\boldsymbol{u}}^+ + \begin{bmatrix}\boldsymbol{c}_\phi\\ \boldsymbol{c}_\upsilon\\ -\boldsymbol{c}_\upsilon\boldsymbol{\kappa}\end{bmatrix}\mathrm{e}^{\boldsymbol{\kappa}}\hat{\boldsymbol{u}}^-=\boldsymbol{0} \qquad \forall\tau, \tag{19}$$

which can be rewritten as $\hat{\boldsymbol{u}}^+=\boldsymbol{R}_{\mathrm{cl}}\mathrm{e}^{\boldsymbol{\kappa}}\hat{\boldsymbol{u}}^-$ with the local reflection coefficient matrix, $\boldsymbol{R}_{\mathrm{cl}}$ defined as:

$$\boldsymbol{R}_{\mathrm{cl}}=-\begin{bmatrix}\boldsymbol{c}_\phi\\ \boldsymbol{c}_\upsilon\\ \boldsymbol{c}_\upsilon\boldsymbol{\kappa}\end{bmatrix}^{-1}\begin{bmatrix}\boldsymbol{c}_\phi\\ \boldsymbol{c}_\upsilon\\ -\boldsymbol{c}_\upsilon\boldsymbol{\kappa}\end{bmatrix} \tag{20}$$

In a similar way, the wave conditions at the free wing tip is written in a form to express the reflection coefficient matrix $\boldsymbol{R}_{\mathrm{fr}}$ such as $\hat{\boldsymbol{u}}^-=\boldsymbol{R}_{\mathrm{fr}}\mathrm{e}^{\boldsymbol{\kappa}}\hat{\boldsymbol{u}}^+$ with

$$\begin{matrix}\phi'(1)=0 & \rightarrow\\ \upsilon''(1)=0 & \rightarrow\\ \upsilon'''(1)=0 & \rightarrow\end{matrix} \qquad \boldsymbol{R}_{\mathrm{fr}}=-\begin{bmatrix}-\boldsymbol{c}_\phi\boldsymbol{\kappa}\\ \boldsymbol{c}_\upsilon\boldsymbol{\kappa}^2\\ -\boldsymbol{c}_\upsilon\boldsymbol{\kappa}^3\end{bmatrix}^{-1}\begin{bmatrix}\boldsymbol{c}_\phi\boldsymbol{\kappa}\\ \boldsymbol{c}_\upsilon\boldsymbol{\kappa}^2\\ \boldsymbol{c}_\upsilon\boldsymbol{\kappa}^3\end{bmatrix} \tag{21}$$

Imposing $\Upsilon = 0$ and $\tilde{e} = 0$ in Eqs. (20) and (21), that is going back to the classical uncoupled beam vibration case, translate to $\bar{X}_1 = X_2 = X_3 = 0$ (i.e. $\boldsymbol{c}_\phi = \begin{bmatrix} 1 & 0 & 0 \end{bmatrix}$ and $\boldsymbol{c}_\upsilon = \begin{bmatrix} 0 & 1 & 1 \end{bmatrix}$) and $\kappa_3 = -\mathrm{i}\kappa_2$. The above reflection coefficient matrices become identical to the more classical reflection matrices given for instance in [27].

2.2.3. Governing equation of motion

Accounting for boundary conditions, the overall governing equation on the wave amplitudes takes the form [7] :

$$\boldsymbol{A}(\lambda, \Upsilon)\boldsymbol{x} = \boldsymbol{0} \tag{22}$$

where

$$\boldsymbol{A} = \begin{bmatrix} \boldsymbol{I} & -\boldsymbol{R}_{\mathrm{cl}}\,\mathrm{e}^{\boldsymbol{\kappa}} \\ -\boldsymbol{R}_{\mathrm{fr}}\,\mathrm{e}^{\boldsymbol{\kappa}} & \boldsymbol{I} \end{bmatrix} \quad \text{and} \quad \boldsymbol{x} = \begin{bmatrix} \hat{\boldsymbol{u}}^+ \\ \hat{\boldsymbol{u}}^- \end{bmatrix}. \tag{23}$$

$\boldsymbol{I}$ is the identity matrix, and the local reflection matrices at the wing ends ($\boldsymbol{R}_{\mathrm{cl}}$ at wing root and $\boldsymbol{R}_{\mathrm{fr}}$ at wingtip) express the ratio of reflected over incoming waves at clamped and free boundary respectively. Both the local reflection matrices and the dispersion matrix are function of the complex frequency λ – via the wavenumbers κ_i, and parametrized by the airspeed Υ. Whereas the wave amplitudes are coupled or not does not change the general form Eq. (22). The coupling between flexural and torsional waves is accounted for in the calculation of the reflection matrices which are function of the $\boldsymbol{c}_\phi$ and $\boldsymbol{c}_\upsilon$ coupling ratios.

Expression (22) is equivalent to the phase closure principle [29] which states that solution of the autonomous vibration problem occur when waves superpose to each other with the same phase after one cycle of propagation and reflection. For instance, the first line of (22) indicates that autonomous solution exist when $\hat{\boldsymbol{u}}^+ = \boldsymbol{R}_{\mathrm{cl}}\,\mathrm{e}^{\boldsymbol{\kappa}}\hat{\boldsymbol{u}}^-$. It simply says that it happens when the positive going wave $\hat{\boldsymbol{u}}^+$ (that originate from the wing root) are equal in amplitude and phase to the negative going wave $\hat{\boldsymbol{u}}^-$ (that originate from the wingtip) which have travelled along a distance 1 (characterized by the $\mathrm{e}^{\boldsymbol{\kappa}}$-matrix) and have been reflected at the wing root boundary ($\boldsymbol{R}_{\mathrm{cl}}$-matrix). A similar behaviour can be observed at the wingtip boundary, expressed via the second line of Eq. (22).

2.3. Numerical methods to solve the nonlinear eigenvalue problem

The autonomous system (9) governing the bending and torsion of the wing has been written in term of small perturbations around a trivial solution, becoming, in a wave-based approach the fundamental equation (22) that characterizes the behaviour of propagating and decaying coupled waves. The solutions of this latter, after being substituted in the wave description (17), defines the dynamical behaviour of a small perturbation in time and space. If one removes the trivial case of $\boldsymbol{x} = \boldsymbol{0}$, the other solutions are found when $\det(\boldsymbol{A}(\lambda, \Upsilon)) = 0$.

For a given Υ-parameter, even thought the physical problem considered is linear, it mathematically ends up in a non-linear transcendental eigenvalue problem in λ, with a structure similar to the one described in [11] or [13]. As expected from the continuum dynamics (wave-based) approach, there are an infinite number of eigenvalues solutions of (22). Going back to the general expression (15), the real part of an eigenvalue solution characterizes the damping of the mode whereas its imaginary part relates to its oscillating frequency. As in classical complex eigenvalue analysis, the system will become unstable when one of its eigenvalue gets a positive real part. The critical flutter speed corresponds to the lowest Υ-value at which this happens.

The main difference to what was studied by Balaji et al. in [13] is that in their case, they were interested in finding the stability of a periodically forced system. Stability analysis was performed by studying the change in sign of $\det(A(\lambda))$ in which the eigenvalue λ solution at the stability transition (i.e. at the bifurcation point) must be a multiple of the forcing frequency. In the aeroelastic investigation considered here, the oscillating frequency of the autonomous perturbed system at the flutter speed is not known a priori.

Bearing in mind that there are an infinite number of eigenvalues for a given Υ, different approaches are possible to determine numerically the flutter speed:

1. The first methodology is to solve the following 2-equations - 2-unknowns (λ_r, λ_i) real system with a Newton-Raphson algorithm while iterating on a fixed value of the airspeed Υ, let say $\bar{\Upsilon}$:

$$\begin{cases} \mathrm{Re}\Big(\det\left(\boldsymbol{A}(\lambda_r + \mathrm{i}\lambda_i, \bar{\Upsilon})\right)\Big) = 0 \\ \mathrm{Im}\Big(\det\left(\boldsymbol{A}(\lambda_r + \mathrm{i}\lambda_i, \bar{\Upsilon})\right)\Big) = 0. \end{cases} \tag{24}$$

   The main steps of the algorithm can be summarized as:
   (a) Initialize the algorithm at $\bar{\Upsilon} = 0$ on the purely imaginary eigenvalues (no damping) closed to the natural frequencies of the first few modes of the system
   (b) Iterate by a slow increase in $\bar{\Upsilon}$; solve Eq. (24) for each $\bar{\Upsilon}$-value using an initialization on the previous solution (similar to a sequential continuation)
   (c) Record the real and imaginary parts of the eigenvalues

   The system becomes unstable as soon as one of the eigenvalue gets a positive real part. This is similar to the p-method [2]: the airspeed is swept and complex eigenvalues are calculated without linearization, but with the existence of an infinite number of eigenvalues due to the continuous wave-based approach.

2. If one is interesting only in the critical speed and not in the general modal damping/frequency vs airspeed behaviour, the second option is to directly look for the point of stability change. To do so, one imposes the real part of the eigenvalue to be zero and solves, again with a Newton-Raphson algorithm, for the 2-unknowns (λ_i, Υ) - 2-equations system

$$\begin{cases} \mathrm{Re}\Big(\det\left(\boldsymbol{A}(\mathrm{i}\lambda_i, \Upsilon)\right)\Big) = 0 \\ \mathrm{Im}\Big(\det\left(\boldsymbol{A}(\mathrm{i}\lambda_i, \Upsilon)\right)\Big) = 0 \end{cases} \tag{25}$$

   The solution of this system directly provides the frequency of the unstable mode at the bifurcation point and the critical speed. The initialisation of the algorithm for this second approach is more tricky for the first simulation but once a solution is obtained, it is always possible to use it as an initial point for the next study when sweeping a parameter. Even though it was not done in the current work, solving Eq. (25) within a path continuation algorithm, using an arc-length correction for instance [30], would most probably be an efficient and robust strategy.

3. Following the approach given in [31], it is also possible to effectuate a more global search by spanning different values for both λ_i and Υ while λ_r is imposed to 0. In this approach the values within the couple (λ_i, Υ) are varied iteratively in a given range and $\det\left(\boldsymbol{A}(\mathrm{i}\lambda_i, \Upsilon)\right)$ is evaluated. Then a contouring method with linear interpolation is used in order to find the zeros line of both the real and imaginary part of the later determinant. The crossings of those lines indicate critical points (flutter and divergence). Direct continuation of the zeros lines via pseudo-arclength techniques, while modifying the modal damping, was also proposed later in [32].

4. There have been some attempts, without success, to rewrite the nonlinear eigenvalue (22) problem in an approximated polynomial form or use a partial spectral decomposition [14, 15, 33, 34] following the hints given in [12]. If successful, it could provide a way to use more standard polynomial eigenvalues algorithm.

For the numerical studies performed in this work, the algorithm explained in the first option, that is solving Eq. (24), was sufficient to create plots of damping and frequency as a function of airspeed. When interested in studying directly the influence of a parameter solely the critical speed, Eq. (25) was used.

2.4. Validation

The wave-based approach detailed in this section is now applied to both the Goland wing [4] and an HALE-type wing [35] for validation; these are standard aeroelastic cases that have been studied by many authors. The numerical geometric and material properties of the wings are given in Table 1. Figure 2 shows the evolution of the real and imaginary part of the first three eigenvalues for both systems. Those are obtained using with what was presented as the first option methodology in Section 2.3.

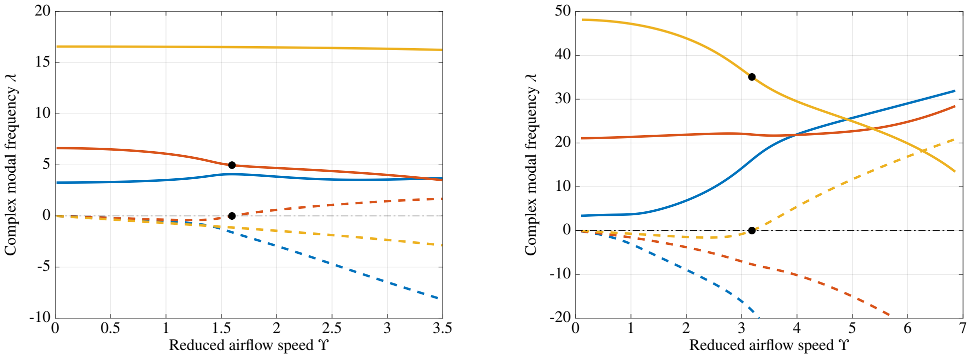

(a) (b)

Figure 2: Real part (dashed lines) and imaginary part (solid lines) of the first three complex eigenvalues solution of Eq. (22), as a function of the reduced airspeed Υ, for (a) the Goland wing and (b) the HALE wing. The flutter speed and associated frequency of the unstable mode are marked with black dots. Unsteady aerodynamics model is used.

The critical flutter speed is defined when one of the eigenvalue gets a positive real part as the airspeed is increased. At this speed, the mode is purely oscillating. Predicted flutter speed and associated frequency, for both test cases, are given in Table 2 and compared with numerical values found in the literature. The given references use different structural models, such as modal approaches based on a typical section with two degrees of freedom only, continuous approximation of the deformed shape via the Rayleigh-Ritz method using bending and torsion shape functions corresponding to the modes of a cantilever Euler-Bernoulli beam, or even more general three-dimensional polynomial approximations. Unsteady aerodynamics modelling is always two-dimensional in the given references – three dimensional model have shown to give sensibly different results [36] showing the importance of three-dimensionnal aerodynamic effects on relatively short span wing, and Theodorsen function is either expressed in the frequency domain or approximated in the time domain. The unstable mode shapes, at the critical flutter speed, are illustrated in Figure 3. These show the bending-torsion coupling behaviour responsible for the instability. The simulated flutter speed and frequency of the Goland wing with quasi-steady aerodynamics assumptions (see Appendix A.1) are also given in Table 2.

It is interesting to note that flutter instability in the HALE wing system mainly originates from the torsion mode whose natural frequency at zero-airspeed is higher than the second bending mode (orange and blue lines in Fig. 2(b), respectively); whereas in the Goland wing, the torsion mode is the overall second mode, that is the red line in Fig. 2(a), and is slightly higher than the first bending mode frequency, again at zero-airspeed. The consequence of this frequency differences between the Goland and the HALE wings is that the mode shape at the critical speed is clearly different between the two cases (see Fig. 3). This will have some impact on the effect of the passive control absorber positioning, as presented in Section 4. The case of the HALE wing design being more complex, because at critical speed, the second bending mode is also involved, it will be chosen as the main test case for evaluating the efficiency of the passive control means.

Table 2: Flutter speed (U_f in $\mathrm{m\,s^{-1}}$) and flutter frequency (ω_f in $\mathrm{rad\,s^{-1}}$) predicted with the proposed wave-based approach and compared to various references, both for the Goland and the HALE wings.

	Goland wing				HALE wing	
	Quasi-steady		Unsteady		Unsteady	
	U_f	ω_f	U_f	ω_f	U_f	ω_f
Present method	35.5	93.8	137.0	70.0	32.5	22.4
Alcorta et al. [23]	35.5	93.9	-	-	-	-
Haddadpoup and Firouz-Abadi [25]	33.5	93.0	136.9	70.0	-	-
Berci [5]	33.6	94.0	136.8	70.0	-	-
Ajaj et al. [37]	-	-	137.0	69.9	33.0	21.7
Ribeiro et al. [38]	-	-	137.5	71.2	32.6	22.6
Patil [35]	-	-	135.6	70.2	32.2	22.6

Structural damping was not included in the above mentioned simulations. Even though any structural damping will increase the speed at which flutter will occur, it is still relevant to quantify this factor in view of comparison with the benefit of adding of a secondary structure as control mean (see Section 3). These results will give reference to assess the effectivness of the different absorbers tested in Section 4. For this matter, the remaining simulations presented in this paper are focused only on the HALE wing under unsteady aerodynamics. Structural damping is included in the formulation via the use of a complex Young's modulus and a loss factor η, therefore affecting the terms EI and GJ in the model (see Table 1) by a factor $(1 + i\eta)$. Figure 4 illustrates the effect of this loss factor when it is varied between 0 and 0.2. Flutter speed increases from $137.0\,\mathrm{m\,s^{-1}}$ to $169.2\,\mathrm{m\,s^{-1}}$, which represents approximatively a 23% increase.

3. Incorporating means of flutter control

In this section, a secondary small structure is added to the wing as an aeroelastic control mean. The originality of this work is to use an anechoic stub in order to delay the critical flutter speed. Its effectiveness will be compare with a more classical tuned-mass-damper system. The equations used to predict the critical speed of both control solutions are given in the subsequent sections.

At the discontinuity created by the attachment location of the secondary system, parametrised by a dimensionless distance $\tilde{p}$ from the wing root $\chi = 0$, the waves that propagate along the wing

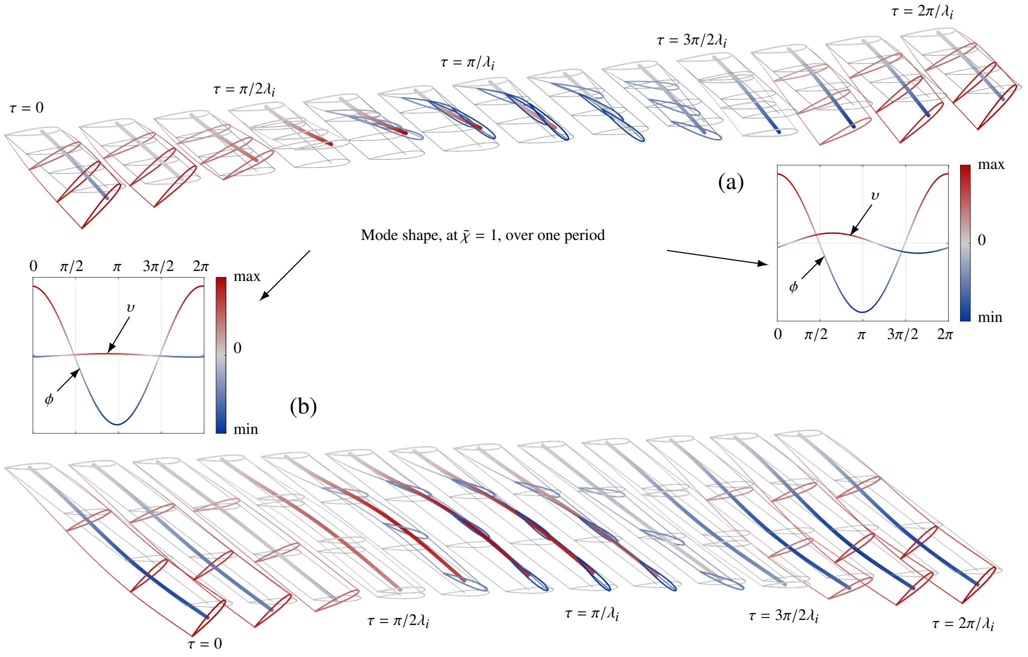

Figure 3: Deformed shape of the unstable mode for the (a) Goland and (b) HALE wings at the critical flutter speed. The corresponding modal frequencies are marked with a black dot in Figure 2. The box insets show the evolution of the wing tip over one period. The color scheme is normalized with respect to the maximum displacement (or rotation) span-wise and over a period. The modes phases are chosen such that $\phi(\chi = 1)$ is maximum at $\tau = 0$.

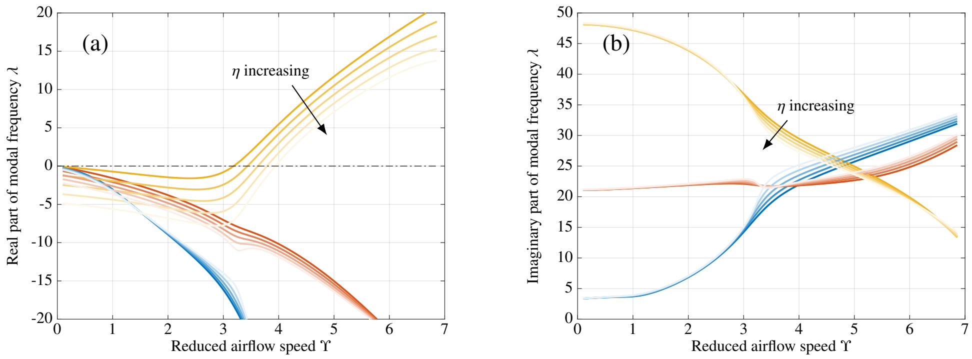

Figure 4: Real (a) and Imaginary (b) parts of the first three complex eigenvalues, as a function of the reduced airspeed Υ. The color scheme shows changes in the wing intrinsic structural damping coefficient, from $\eta = 0$ in dark color to $\eta = 0.15$ in light color.

are partially transmitted and reflected. A particular attention is then made in this section on calculating the associated local reflection/transmission matrix that characterize this behavior. At the position $\chi = \tilde{p}$, the wing is split into two beam elements, noted [1] and [2]. On each of them, the dynamics is modelled using the wave approach described in Section 2 and with a local reference frame. The element number will be added in the notation to characterize the relation between the different variables and a particular beam elements. The waves on elements [1] and [2] travel along a distance $\tilde{p}$ and $1 - \tilde{p}$ respectively.

3.1. Tuned-mass-damper

The first control system studied consists of a mass-damper-spring system, parametrized by the coefficients m_{T}, c_{T}, and k_{T}, attached to the main beam at the dimensionless position $\chi = \tilde{p}$ along the span and offset of a dimensionless distance $\tilde{d}$ chordwise. The later is made dimensionless with respect to the semi-chord b and is defined positive when the absorber is positioned towards the leading edge. Particular values that will be useful for later analysis are $\tilde{d} = 0$: the absorber is attached to the elastic axis, $\tilde{d} = 1 + \tilde{a}$ (or $\tilde{d} - \tilde{a} = 1$): the absorber is located at the leading edge; and $\tilde{d} = -1 + \tilde{a}$ (or $\tilde{d} - \tilde{a} = -1$): the absorber is located at the trailing edge. The model is illustrated in Figure 5. This absorber acts in the transverse direction only. The displacement of the attached mass is parametrized by the dimensionless variable $\delta(\tau)$. The absorber mainly focuses on bending vibration mitigation but does also have a direct effect on the torsion mode due to its offset in the chordwise direction.

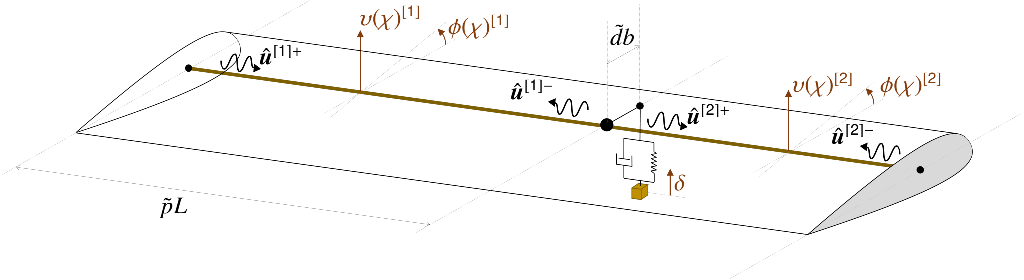

Figure 5: Wave-based model of a wing with an attached tuned-mass-damper.

Splitting the wing in two components at the discontinuity created by the attached mass, the fundamental governing equation using a wave-based approach (22) – i.e. the non-linear eigen value problem to solve in order to estimate the flutter speed – becomes:

$$\boldsymbol{A}(\lambda, \Upsilon)\boldsymbol{x} = \begin{bmatrix} \boldsymbol{I} & -\boldsymbol{R}_{\mathrm{cl}}\mathrm{e}^{\boldsymbol{\kappa}\tilde{p}} & \boldsymbol{0} & \boldsymbol{0} & \boldsymbol{0} \\ -\boldsymbol{\beta}\mathrm{e}^{\boldsymbol{\kappa}\tilde{p}} & \boldsymbol{I} & \boldsymbol{0} & -\boldsymbol{\Pi}\mathrm{e}^{\boldsymbol{\kappa}(1-\tilde{p})} & \boldsymbol{0} \\ -\boldsymbol{\Pi}\mathrm{e}^{\boldsymbol{\kappa}\tilde{p}} & \boldsymbol{0} & \boldsymbol{I} & -\boldsymbol{\beta}\mathrm{e}^{\boldsymbol{\kappa}(1-\tilde{p})} & \boldsymbol{0} \\ \boldsymbol{0} & \boldsymbol{0} & -\boldsymbol{R}_{\mathrm{fr}}\mathrm{e}^{\boldsymbol{\kappa}(1-\tilde{p})} & \boldsymbol{I} & \boldsymbol{0} \\ -\boldsymbol{\tau}\mathrm{e}^{\boldsymbol{\kappa}\tilde{p}} & \boldsymbol{0} & \boldsymbol{0} & -\boldsymbol{\tau}\mathrm{e}^{\boldsymbol{\kappa}(1-\tilde{p})} & \boldsymbol{I} \end{bmatrix} \begin{bmatrix} \hat{\boldsymbol{u}}^{[1]+} \\ \hat{\boldsymbol{u}}^{[1]-} \\ \hat{\boldsymbol{u}}^{[2]+} \\ \hat{\boldsymbol{u}}^{[2]-} \\ \delta \end{bmatrix} = \boldsymbol{0} \tag{26}$$

The identification of the local transmission/reflection coefficient matrices ($\boldsymbol{\Pi}$, $\boldsymbol{\beta}$ and $\boldsymbol{\tau}$), which appear in the $\boldsymbol{A}$-matrix expression of Eq. (26), is explained next.

They are obtained using forces equilibrium and displacement continuity at the absorber attachment point[4]. In a dimensionless form, those are:

$$\begin{aligned}
&\phi(\tilde{p})^{[1]} - \phi(0)^{[2]} = 0, \qquad \upsilon(\tilde{p})^{[1]} - \upsilon(0)^{[2]} = 0, \qquad \upsilon'(\tilde{p})^{[1]} - \upsilon'(0)^{[2]} = 0,\\
&\phi'(\tilde{p})^{[1]} - \phi'(0)^{[2]} + \frac{\tilde{k}_{\mathrm{T}}\tilde{d}\tilde{b}}{\gamma}\Big(\upsilon(\tilde{p})^{[1]} + \tilde{d}\tilde{b}\phi(\tilde{p})^{[1]} - \delta\Big) + \frac{\tilde{c}_{\mathrm{T}}\tilde{d}\tilde{b}}{\gamma}\Big(\upsilon(\tilde{p})^{[1]} + \tilde{d}\tilde{b}\phi(\tilde{p})^{[1]} - \delta\Big)\lambda = 0,\\
&\upsilon''(\tilde{p})^{[1]} - \upsilon''(0)^{[2]} = 0,\\
&-\upsilon'''(\tilde{p})^{[1]} + \upsilon'''(0)^{[2]} + \tilde{k}_{\mathrm{T}}\Big(\upsilon(\tilde{p})^{[1]} + \tilde{d}\tilde{b}\phi(\tilde{p})^{[1]} - \delta\Big) + \tilde{c}_{\mathrm{T}}\Big(\upsilon(\tilde{p})^{[1]} + \tilde{d}\tilde{b}\phi(\tilde{p})^{[1]} - \delta\Big)\lambda = 0,\\
&-\upsilon'''(\tilde{p})^{[1]} + \upsilon'''(0)^{[2]} + \tilde{m}_{\mathrm{T}}\delta\lambda^2 = 0 \qquad\qquad \forall\tau.
\end{aligned} \tag{27}$$

The dimensionless parameters of the attached mass are

$$\tilde{m}_{\mathrm{T}} = \frac{m_{\mathrm{T}}}{mL}, \qquad \tilde{c}_{\mathrm{T}} = \frac{c_{\mathrm{T}}T}{mL}, \qquad \tilde{k}_{\mathrm{T}} = \frac{k_{\mathrm{T}}T^2}{mL}. \tag{28}$$

The dimensionless parameter $\tilde{m}_{\mathrm{T}}$ expresses the ratio between the mass of the attached absorber and that of the whole beam. It will be used in the simulation presented in Section 4 to characterise the efficiency of the absorber with regards to increasing the critical flutter speed.

Substituting the general wave form solution (17) in Eq. (27) in terms of the variables ϕ and υ, and separating the created waves amplitudes to the incident waves amplitudes, the different equations that characterize the discontinuity can be rewritten under the following matrix form (similar to the one used at boundaries, see Eq. (18)):

$$\boldsymbol{C}\begin{bmatrix}\hat{\boldsymbol{u}}^{[1]-}\\ \hat{\boldsymbol{u}}^{[2]+}\\ \delta\end{bmatrix} + \boldsymbol{H}\begin{bmatrix}\mathrm{e}^{\boldsymbol{\kappa}\tilde{p}} & \boldsymbol{0}\\ \boldsymbol{0} & \mathrm{e}^{\boldsymbol{\kappa}(1-\tilde{p})}\end{bmatrix}\begin{bmatrix}\hat{\boldsymbol{u}}^{[1]+}\\ \hat{\boldsymbol{u}}^{[2]-}\end{bmatrix} = \boldsymbol{0}, \quad \text{with}$$

$$\boldsymbol{C} = \begin{bmatrix}
\boldsymbol{c}_\phi & -\boldsymbol{c}_\phi & 0\\
\boldsymbol{c}_\upsilon & -\boldsymbol{c}_\upsilon & 0\\
-\boldsymbol{c}_\upsilon\boldsymbol{\kappa} & -\boldsymbol{c}_\upsilon\boldsymbol{\kappa} & 0\\
\boldsymbol{c}_\phi\boldsymbol{\kappa} - \tilde{f}(\boldsymbol{c}_\upsilon + \tilde{d}\tilde{b}\boldsymbol{c}_\phi) & \boldsymbol{c}_\phi\boldsymbol{\kappa} & \tilde{f}\\
-\boldsymbol{c}_\upsilon\boldsymbol{\kappa}^2 & \boldsymbol{c}_\upsilon\boldsymbol{\kappa}^2 & 0\\
\boldsymbol{c}_\upsilon\boldsymbol{\kappa}^3 + \tilde{g}(\boldsymbol{c}_\upsilon + \tilde{d}\tilde{b}\boldsymbol{c}_\phi) & \boldsymbol{c}_\upsilon\boldsymbol{\kappa}^3 & -\tilde{g}\\
\boldsymbol{c}_\upsilon\boldsymbol{\kappa}^3 & \boldsymbol{c}_\upsilon\boldsymbol{\kappa}^3 & \tilde{m}_{\mathrm{T}}\lambda^2
\end{bmatrix}, \quad
\boldsymbol{H} = \begin{bmatrix}
\boldsymbol{c}_\phi & -\boldsymbol{c}_\phi\\
\boldsymbol{c}_\upsilon & -\boldsymbol{c}_\upsilon\\
\boldsymbol{c}_\upsilon\boldsymbol{\kappa} & \boldsymbol{c}_\upsilon\boldsymbol{\kappa}\\
-\boldsymbol{c}_\phi\boldsymbol{\kappa} - \tilde{f}(\boldsymbol{c}_\upsilon + \tilde{d}\tilde{b}\boldsymbol{c}_\phi) & -\boldsymbol{c}_\phi\boldsymbol{\kappa}\\
-\boldsymbol{c}_\upsilon\boldsymbol{\kappa}^2 & \boldsymbol{c}_\upsilon\boldsymbol{\kappa}^2\\
-\boldsymbol{c}_\upsilon\boldsymbol{\kappa}^3 + \tilde{g}(\boldsymbol{c}_\upsilon + \tilde{d}\tilde{b}\boldsymbol{c}_\phi) & -\boldsymbol{c}_\upsilon\boldsymbol{\kappa}^3\\
-\boldsymbol{c}_\upsilon\boldsymbol{\kappa}^3 & -\boldsymbol{c}_\upsilon\boldsymbol{\kappa}^3
\end{bmatrix} \tag{29}$$

$\tilde{f} = \tilde{g}\tilde{d}\tilde{b}/\gamma$ and $\tilde{g} = \tilde{k}_{\mathrm{T}} + \tilde{c}_{\mathrm{T}}\lambda$. The row order in Eq. (29) follows the order of the equations given in (27). The relationship between transmitted/reflected waves and incident waves defines the local transmission/reflection coefficients matrices. For this matter, Eq. (29) is rewritten as

$$\begin{bmatrix}\hat{\boldsymbol{u}}^{[1]-}\\ \hat{\boldsymbol{u}}^{[2]+}\\ \delta\end{bmatrix} = \boldsymbol{T}_{\mathrm{T}}\begin{bmatrix}\mathrm{e}^{\boldsymbol{\kappa}\tilde{p}} & \boldsymbol{0}\\ \boldsymbol{0} & \mathrm{e}^{\boldsymbol{\kappa}(1-\tilde{p})}\end{bmatrix}\begin{bmatrix}\hat{\boldsymbol{u}}^{[1]+}\\ \hat{\boldsymbol{u}}^{[2]-}\end{bmatrix} \tag{30}$$

with

$$\boldsymbol{T}_{\mathrm{T}} = -\boldsymbol{C}^{-1}\boldsymbol{H} = \begin{bmatrix}\boldsymbol{\beta} & \boldsymbol{\Pi}\\ \boldsymbol{\Pi} & \boldsymbol{\beta}\\ \boldsymbol{\tau} & \boldsymbol{\tau}\end{bmatrix}.$$

---

[4] A similar development was made for a non-linear absorber attached to a purely bending beam in [39].

These local transmission/reflection matrices are function of the modal frequency, the airspeed (within the calculation of the wavenumbers) and the different parameters of the wing and attached mass. The properties of the later will be numerically evaluated in order to *tune* it to the unstable frequency in the applications presented in Section 4. The next section presents another possible strategy to postpone flutter speed that will later be confronted to the TMD system.

3.2. Anechoic stub

3.2.1. Wave-based modelling of the stub

One of the objective of the current paper is to analyse the efficiency on aeroelastic effects mitigation of the concept used by Lv and Leamy in [40] as a mean of damping an harmonically excited structure. It consists on an anechoic termination incorporated at the end of a small secondary beam structure, then called *anechoic stub*, attached to the primary structure.

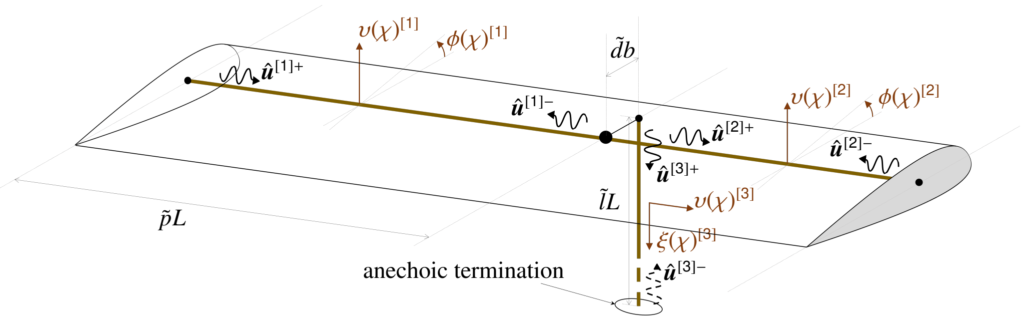

Figure 6: Wave-based model of a wing with an attached anechoic stub.

The secondary structure is modelled as an additional beam element, noted [3] whose kinematics is assumed to be restricted to in-plane bending and longitudinal displacements. It is connected to the main wing at $\chi = \tilde{p}$ and offset chordwise from the elastic axis by a dimensionless distance $\tilde{d}$. Its kinematics is characterized by the dimensionless parameters $\upsilon = w^{[3]}/L$ and $\xi = u^{[3]}/L$, where $w^{[3]}$ and $u^{[3]}$ correspond to the transverse and longitudinal displacements of the stub (see Fig. 6). The superscript [3] is for the moment omitted in υ and ξ for simplification but it will be reconsidered when coupling the different beam elements. For consistency in the equations and facilitating the coupling expressions, the adimensionning is performed with reference to the wing geometry and dynamics, i.e. the nondimensional time and space are identical as those used in the previous sections. The dimensionless equations of motion of this element are:

$$\tilde{m}_{\mathrm{A}}\ddot{\xi} - \sigma_l \tilde{l}\xi'' = 0 \tag{31a}$$

$$\tilde{m}_{\mathrm{A}}\ddot{\upsilon} + \sigma_f \tilde{l}\upsilon'''' = 0, \tag{31b}$$

where $\tilde{m}_{\mathrm{A}}$ is the ratio of the mass of the anechoic stub over the mass (mL) of the wing, σ_l is the ratio of the axial stiffness of the stub over the rotational stiffness (EI/L^2) of the wing, σ_f is the ratio of the flexural rigidity of the stub over that of the wing (EI), and the dimensionless length $\tilde{l}$ is defined as the ratio of the stub length with that of the wing.

Using a wave propagation approach in the stub, the displacements ξ and υ are written, in a local frame originating at its connection with the wing, in a form similar to that given in (17):

$$\begin{bmatrix} \xi \\ \upsilon \end{bmatrix} (\chi, \tau) = \begin{bmatrix} \boldsymbol{c}_{\xi} \\ \boldsymbol{c}_{\upsilon,\mathrm{A}} \end{bmatrix} \begin{bmatrix} \mathrm{e}^{\boldsymbol{\kappa}_{\mathrm{A}}\chi} & \mathrm{e}^{\boldsymbol{\kappa}_{\mathrm{A}}(\tilde{l}-\chi)} \end{bmatrix} \begin{bmatrix} \hat{\boldsymbol{u}}^{[3]+} \\ \hat{\boldsymbol{u}}^{[3]-} \end{bmatrix} \mathrm{e}^{\lambda\tau} + \text{c.c}, \tag{32}$$

with

$$\boldsymbol{c}_{\xi} = \begin{bmatrix} 1 & 0 & 0 \end{bmatrix} \quad \text{and} \quad \boldsymbol{c}_{\upsilon,\mathrm{A}} = \begin{bmatrix} 0 & 1 & 1 \end{bmatrix}.$$

The flexural and longitudinal displacements are uncoupled. The wave amplitude vectors $\hat{\boldsymbol{u}}^{[3]\pm}$ contain the amplitude of longitudinal propagating wave, flexural far-field propagative wave and flexural near-field decaying wave, in such order, propagating in the positive and negative χ-directions. As the frequency λ is a complex number, these waves are however neither purely propagating or decaying. The diagonal wavenumber matrix $\boldsymbol{\kappa}_{\mathrm{A}}$ contains the dimensionless wavenumbers associated to the above mentioned waves. They are found by solving the dispersion relation related to Eq. (31). These equations are standard and so are the wavenumbers but, as the frequency λ is generally complex-valued, the choice of which wavenumber solution to keep with regards to the formulation (32) must be done attentively. The six wavenumbers solutions are

$$\kappa_i = \pm\sqrt{\lambda^2 \frac{\tilde{m}_{\mathrm{A}}}{\sigma_l \tilde{l}}} \quad \text{or} \quad \kappa_i = \pm\sqrt{\pm \mathrm{i}\lambda\sqrt{\frac{\tilde{m}_{\mathrm{A}}}{\sigma_f \tilde{l}}}}. \tag{33}$$

Using the same rule as what was explained in Section 2.2.1, one only keeps those whose phase velocity (see Eq. (14)) is positive.

The attachment of the anechoic stub on the main beam creates two new discontinuities that affect the propagation of waves:

1. The joint in $\chi = \tilde{p}$ behaves like a T-joint at which three beam elements are attached to each other. This kind of connection was treated with a wave-based approach for instance in [27, 40, 41]. However determining the influence of the joint on the waves behaviour is here slightly different from the one modelled in the above references because of the bending/torsion coupling existing in the main beam. Its characteristic equations will be derived in Section 3.2.2.
2. The anechoic stub termination is designed to attenuate waves and reflect as little waves as possible. It is parametrized by a reflection coefficient $\tilde{r}$, see Section 3.2.3. Modelling accurately the wave behaviour at the termination is beyond the scope of this paper which focus on the effectiveness of such concept to postpone flutter speed. In an ideal termination, $\tilde{r}$ will be zero. However, depending on the anechoic stub design and the technology used (purely passive, semi-active, etc.), this coefficient can vary from very small (approximatively 0.1) [21, 42] up to close to one as if it was almost inexistent. In any case, this coefficient decreases with increased frequency, i.e.the wave absorption is more efficient at higher frequency. Different values will be used in the simulations presented in Section 4.

Accounting for the boundary conditions of the wing, the absorbing termination of the stub and the local transmission matrix that characterizes the T-joint between the main beam and the stub, the whole dynamics of the system can be described under the same form of non-linear eigenvalue problem: $\boldsymbol{A}(\lambda, \Upsilon)\boldsymbol{x} = \boldsymbol{0}$, with

$$\boldsymbol{A} = \begin{bmatrix} \boldsymbol{I} & -\boldsymbol{R}_{\mathrm{cl}}\mathrm{e}^{\boldsymbol{\kappa}\tilde{p}} & \boldsymbol{0} & \boldsymbol{0} & \boldsymbol{0} & \boldsymbol{0} \\ -\boldsymbol{\beta}\mathrm{e}^{\boldsymbol{\kappa}\tilde{p}} & \boldsymbol{I} & \boldsymbol{0} & -\boldsymbol{\Pi}\mathrm{e}^{\boldsymbol{\kappa}(1-\tilde{p})} & \boldsymbol{0} & -\boldsymbol{\Pi}_{31}\mathrm{e}^{\boldsymbol{\kappa}_{\mathrm{A}}\tilde{l}} \\ -\boldsymbol{\Pi}\mathrm{e}^{\boldsymbol{\kappa}\tilde{p}} & \boldsymbol{0} & \boldsymbol{I} & -\boldsymbol{\beta}\mathrm{e}^{\boldsymbol{\kappa}(1-\tilde{p})} & \boldsymbol{0} & -\boldsymbol{\Pi}_{32}\mathrm{e}^{\boldsymbol{\kappa}_{\mathrm{A}}\tilde{l}} \\ \boldsymbol{0} & \boldsymbol{0} & -\boldsymbol{R}_{\mathrm{fr}}\mathrm{e}^{\boldsymbol{\kappa}(1-\tilde{p})} & \boldsymbol{I} & \boldsymbol{0} & \boldsymbol{0} \\ -\boldsymbol{\Pi}_{13}\mathrm{e}^{\boldsymbol{\kappa}\tilde{p}} & \boldsymbol{0} & \boldsymbol{0} & -\boldsymbol{\Pi}_{23}\mathrm{e}^{\boldsymbol{\kappa}(1-\tilde{p})} & \boldsymbol{I} & -\boldsymbol{\beta}_3\mathrm{e}^{\boldsymbol{\kappa}_{\mathrm{A}}\tilde{l}} \\ \boldsymbol{0} & \boldsymbol{0} & \boldsymbol{0} & \boldsymbol{0} & -\boldsymbol{R}_{\infty}\mathrm{e}^{\boldsymbol{\kappa}_{\mathrm{A}}\tilde{l}} & \boldsymbol{I} \end{bmatrix} \tag{34}$$

and

$$\boldsymbol{x} = \begin{bmatrix} \hat{\boldsymbol{u}}^{[1]+} \\ \hat{\boldsymbol{u}}^{[1]-} \\ \hat{\boldsymbol{u}}^{[2]+} \\ \hat{\boldsymbol{u}}^{[2]-} \\ \hat{\boldsymbol{u}}^{[3]+} \\ \hat{\boldsymbol{u}}^{[3]-} \end{bmatrix}$$

The expressions of the local transmission/reflection matrices that appear in the above $\boldsymbol{A}$-matrix are detailed in the next two sections, in turn for the T-joint and for the anechoic end.

3.2.2. T joint

We assume that the longitudinal displacement in the wing is negligible and the axial stiffness is infinite. The T-joint then connects two beam-like wing elements [i] ([i] = [1], [2]) whose kinematics is in bending $\upsilon^{[i]}$ and torsion $\phi^{[i]}$, and a beam stub element [3] whose kinematics is in bending $\upsilon^{[3]}$ and longitudinal $\xi^{[3]}$ motion. The governing equations, displacement and slope continuity, and force and moment equilibrium, of the T-joint at the connection between the different elements are:

$$\begin{aligned}
&\phi(\tilde{p})^{[1]} - \phi(0)^{[2]} = 0, \qquad \upsilon(\tilde{p})^{[1]} - \upsilon(0)^{[2]} = 0, \qquad \upsilon'(\tilde{p})^{[1]} - \upsilon'(0)^{[2]} = 0,\\
&\upsilon(\tilde{p})^{[1]} + \tilde{d}\tilde{b}\phi(\tilde{p})^{[1]} + \xi(0)^{[3]} = 0 \qquad \upsilon'(\tilde{p})^{[1]} - \upsilon'(0)^{[3]} = 0, \qquad \upsilon(0)^{[3]} = 0,\\
&\phi'(\tilde{p})^{[1]} - \phi'(0)^{[2]} + \tilde{d}\tilde{b}\sigma_t\xi'(0)^{[3]} = 0, \qquad -\upsilon''(\tilde{p})^{[1]} + \upsilon''(0)^{[2]} + \sigma_f\upsilon''(0)^{[3]} = 0,\\
&\upsilon'''(\tilde{p})^{[1]} - \upsilon'''(0)^{[2]} - \sigma_l\xi'(0)^{[3]} = 0 \qquad \forall\tau
\end{aligned} \tag{35}$$

In the previous equation, σ_t denotes the ratio of the axial stiffness of the stub over the effective torsional stiffness (GJ/L^2) of the wing.

In the same order, the above equations give the following relationship between incident and reflected/transmitted waves

$$\boldsymbol{C}\begin{bmatrix} \hat{\boldsymbol{u}}^{[1]-} \\ \hat{\boldsymbol{u}}^{[2]+} \\ \hat{\boldsymbol{u}}^{[3]+} \end{bmatrix} + \boldsymbol{H}\begin{bmatrix} \mathrm{e}^{\boldsymbol{\kappa}\tilde{p}} & \boldsymbol{0} & \boldsymbol{0} \\ \boldsymbol{0} & \mathrm{e}^{\boldsymbol{\kappa}(1-\tilde{p})} & \boldsymbol{0} \\ \boldsymbol{0} & \boldsymbol{0} & \mathrm{e}^{\boldsymbol{\kappa}_\mathrm{A}\tilde{l}} \end{bmatrix}\begin{bmatrix} \hat{\boldsymbol{u}}^{[1]+} \\ \hat{\boldsymbol{u}}^{[2]-} \\ \hat{\boldsymbol{u}}^{[3]-} \end{bmatrix} = \boldsymbol{0}$$

$$\text{with } \boldsymbol{C} = \begin{bmatrix} \boldsymbol{c}_\phi & -\boldsymbol{c}_\phi & \boldsymbol{0} \\ \boldsymbol{c}_\upsilon & -\boldsymbol{c}_\upsilon & \boldsymbol{0} \\ -\boldsymbol{c}_\upsilon\boldsymbol{\kappa} & -\boldsymbol{c}_\upsilon\boldsymbol{\kappa} & \boldsymbol{0} \\ \boldsymbol{c}_\upsilon + \tilde{d}\tilde{b}\boldsymbol{c}_\phi & \boldsymbol{0} & \boldsymbol{c}_\xi \\ -\boldsymbol{c}_\upsilon\boldsymbol{\kappa} & \boldsymbol{0} & -\boldsymbol{c}_{\upsilon,\mathrm{A}}\boldsymbol{\kappa}_\mathrm{A} \\ \boldsymbol{0} & \boldsymbol{0} & \boldsymbol{c}_{\upsilon,\mathrm{A}} \\ -\boldsymbol{c}_\phi\boldsymbol{\kappa} & -\boldsymbol{c}_\phi\boldsymbol{\kappa} & \tilde{d}\tilde{b}\sigma_t\boldsymbol{c}_\xi\boldsymbol{\kappa}_\mathrm{A} \\ -\boldsymbol{c}_\upsilon\boldsymbol{\kappa}^2 & \boldsymbol{c}_\upsilon\boldsymbol{\kappa}^2 & \sigma_f\boldsymbol{c}_{\upsilon,\mathrm{A}}\boldsymbol{\kappa}_\mathrm{A}^2 \\ -\boldsymbol{c}_\upsilon\boldsymbol{\kappa}^3 & -\boldsymbol{c}_\upsilon\boldsymbol{\kappa}^3 & -\sigma_l\boldsymbol{c}_\xi\boldsymbol{\kappa}_\mathrm{A} \end{bmatrix}, \quad \boldsymbol{H} = \begin{bmatrix} \boldsymbol{c}_\phi & -\boldsymbol{c}_\phi & \boldsymbol{0} \\ \boldsymbol{c}_\upsilon & -\boldsymbol{c}_\upsilon & \boldsymbol{0} \\ \boldsymbol{c}_\upsilon\boldsymbol{\kappa} & \boldsymbol{c}_\upsilon\boldsymbol{\kappa} & \boldsymbol{0} \\ \boldsymbol{c}_\upsilon + \tilde{d}\tilde{b}\boldsymbol{c}_\phi & \boldsymbol{0} & \boldsymbol{c}_\xi \\ \boldsymbol{c}_\upsilon\boldsymbol{\kappa} & \boldsymbol{0} & \boldsymbol{c}_{\upsilon,\mathrm{A}}\boldsymbol{\kappa}_\mathrm{A} \\ \boldsymbol{0} & \boldsymbol{0} & \boldsymbol{c}_{\upsilon,\mathrm{A}} \\ \boldsymbol{c}_\phi\boldsymbol{\kappa} & \boldsymbol{c}_\phi\boldsymbol{\kappa} & -\tilde{d}\tilde{b}\sigma_t\boldsymbol{c}_\xi\boldsymbol{\kappa}_\mathrm{A} \\ -\boldsymbol{c}_\upsilon\boldsymbol{\kappa}^2 & \boldsymbol{c}_\upsilon\boldsymbol{\kappa}^2 & \sigma_f\boldsymbol{c}_{\upsilon,\mathrm{A}}\boldsymbol{\kappa}_\mathrm{A}^2 \\ \boldsymbol{c}_\upsilon\boldsymbol{\kappa}^3 & \boldsymbol{c}_\upsilon\boldsymbol{\kappa}^3 & \sigma_l\boldsymbol{c}_\xi\boldsymbol{\kappa}_\mathrm{A} \end{bmatrix} \tag{36}$$

The last equation can be rewritten as

$$\begin{bmatrix} \hat{\boldsymbol{u}}^{[1]-} \\ \hat{\boldsymbol{u}}^{[2]+} \\ \hat{\boldsymbol{u}}^{[3]+} \end{bmatrix} = \boldsymbol{T}_\mathrm{A}\begin{bmatrix} \mathrm{e}^{\boldsymbol{\kappa}\tilde{p}} & \boldsymbol{0} & \boldsymbol{0} \\ \boldsymbol{0} & \mathrm{e}^{\boldsymbol{\kappa}(1-\tilde{p})} & \boldsymbol{0} \\ \boldsymbol{0} & \boldsymbol{0} & \mathrm{e}^{\boldsymbol{\kappa}_\mathrm{A}\tilde{l}} \end{bmatrix}\begin{bmatrix} \hat{\boldsymbol{u}}^{[1]+} \\ \hat{\boldsymbol{u}}^{[2]-} \\ \hat{\boldsymbol{u}}^{[3]-} \end{bmatrix} \tag{37}$$

with

$$\boldsymbol{T}_{\mathrm{A}} = -\boldsymbol{C}^{-1}\boldsymbol{H} = \begin{bmatrix} \boldsymbol{\beta} & \boldsymbol{\Pi} & \boldsymbol{\Pi}_{31} \\ \boldsymbol{\Pi} & \boldsymbol{\beta} & \boldsymbol{\Pi}_{32} \\ \boldsymbol{\Pi}_{13} & \boldsymbol{\Pi}_{23} & \boldsymbol{\beta}_3 \end{bmatrix}.$$

The coefficients of the $\boldsymbol{T}_{\mathrm{A}}$ matrix are placed in the corresponding coupling terms of the overall $\boldsymbol{A}$ matrix (see Eq. (34)).

3.2.3. Absorbing termination

With the wave-based approach detailed in Section 3.2.1 (see Eq. (34)), the stub termination is characterized by a reflection matrix, noted $\boldsymbol{R}_\infty$ that is defined by the following expression

$$\hat{\boldsymbol{u}}^{[3]-} = \boldsymbol{R}_\infty \mathrm{e}^{\kappa_{\mathrm{A}}\tilde{l}}\hat{\boldsymbol{u}}^{[3]+} \tag{38}$$

where $\boldsymbol{R}_\infty$ represents the reflection matrix at a free end multiplied by $\tilde{r}$. The former can be obtained using equations similar to the one used to obtain $\boldsymbol{R}_{\mathrm{fr}}$ (see Section 2.2.2) that simply represent a free boundary in case of longitudinal and flexural vibration :

$$\boldsymbol{R}_\infty = -\tilde{r}\begin{bmatrix} -\boldsymbol{c}_\xi\kappa_{\mathrm{A}} \\ \boldsymbol{c}_{\upsilon,\mathrm{A}}\kappa_{\mathrm{A}}^2 \\ -\boldsymbol{c}_{\upsilon,\mathrm{A}}\kappa_{\mathrm{A}}^3 \end{bmatrix}^{-1}\begin{bmatrix} \boldsymbol{c}_\xi\kappa_{\mathrm{A}} \\ \boldsymbol{c}_{\upsilon,\mathrm{A}}\kappa_{\mathrm{A}}^2 \\ \boldsymbol{c}_{\upsilon,\mathrm{A}}\kappa_{\mathrm{A}}^3 \end{bmatrix} = \tilde{r}\begin{bmatrix} 1 & 0 & 0 \\ 0 & -\mathrm{i} & 1+\mathrm{i} \\ 0 & 1-\mathrm{i} & \mathrm{i} \end{bmatrix}. \tag{39}$$

4. Results on Flutter mitigation simulation

The previous sections introduced two different damping mechanisms that could be used to postpone the critical flutter speed. This section evaluates their effectiveness numerically by varying different design parameters. These parameters are many and include the absorber geometrical and mass properties as well as its position relatively to the wing. A proper optimisation study with all these inputs is beyond the scope of this work. Here we solely focus on getting general trends to obtain a better insights of the physics involved.

First, the used of a Tuned-mass-damper is investigated, then we will focus on the anechoic stub made as an additional appendix with and anechoic termination. Except explicitly said otherwise, the wing geometry tested corresponds to the HALE wing whose parameters are given in Table 1.

4.1. Use of the Tuned-Mass-Damper

In mitigating linear resonant systems, a TMD is efficient when its properties in stiffness and damping are properly *tuned*. It is well known that the presence of the TMD creates two smaller-amplitude peaks. The usual way to parametrize the TMD is first to fix the mass to a small percentage of the overall modal mass associated with the frequency to mitigate, then to tune the absorber stiffness such its natural frequency matches approximately that of the primary structure, and finally to set the linear viscous damping coefficient so that the damping ratio, called $\xi_{\mathrm{T}} = c_{\mathrm{T}}/(2\sqrt{k_{\mathrm{T}}m_{\mathrm{T}}})$, is such that both peaks created by the presence of the TMD have the same amplitude and therefore maximize the energy absorbed. The optimal parameters values of the

TMD made on the *equal-peaks* method are given in closed form expressions for instance in [43]. The optimal damping ratio, noted ξ_{T}^{*}, is:

$$\xi_{\text{T}}^{*} = \frac{1}{4}\sqrt{\frac{8 + 9\tilde{m}_{\text{T}} - 4\sqrt{4 + 3\tilde{m}_{\text{T}}}}{1 + \tilde{m}_{\text{T}}}}, \tag{40}$$

where $\tilde{m}_{\text{T}}$ is the mass ratio. This specific damping ratio value will be used in most of the simulations presented in this section.

In the context of this paper, one does not look for mitigating a resonant system but an unstable one. The TMD stiffness should then be tuned in order to target the frequency of the unstable flutter mode at the critical speed. However, as both the critical speed and the unstable frequency depend on the TMD intrinsic parameters, it is relatively tricky to get an optimal value. The position of the TMD along the wing, spanwise and chordwise, also influence the overall dynamics. The following section will investigate in turn, each of these parameters, hoping to obtain some general design rules for a better efficiency. The increase in flutter speed will also serve as a baseline to evaluate the effectivness of the anechoic stub in Section 4.2.

4.1.1. Influence of the TMD stiffness and damping

The coupled influence of both the stiffness and the damping value of the TMD on the critical flutter speed, and that for several TMD masses, is first studied. For this matter, the chordwise position of the TMD is first imposed to be on the wing elastic axis (i.e. $\tilde{d} = 0$) in order to avoid a direct influence on the torsion mode and simplify interpretation of results. The TMD if fixed at a position $\tilde{p} = 0.77$ spanwise – this zone, approximatively 3/4 spanwise is of particular interest for the HALE wing, as it will be discussed later.

The results of this first parameter study are illustrated in Fig. 7. It shows the ratio of the flutter speed compared to that of the clean wing baseline flutter speed as a function of the TMD frequency $\tilde{\omega}_{\text{T}} = \sqrt{\tilde{k}_{\text{T}}/\tilde{m}_{\text{T}}}$ and damping ratio ξ_{T} for two particular mass ratios ($\tilde{m}_{\text{T}} = 0.05$ in Fig. 7(a) and $\tilde{m}_{\text{T}} = 0.01$ in Fig. 7(b)). The clean wing flutter speed, noted Υ_f^o, relates to the wing without any secondary structure and was found to be $\Upsilon_f^o = 3.19$ (equivalent to $U_f = 32.5\,\text{m}\,\text{s}^{-1}$ given in Table 2). A striking feature in both mass ratio plots is the "danger zone" around a reduced frequency of $\tilde{\omega}_{\text{T}} \approx 40$ and low damping, where the critical flutter speed is significantly reduced (down to $\Upsilon_f/\Upsilon_f^o \approx 0.83$) compared to the case without absorber. In this configuration, the additional mass destabilizes the system without adding any damping.

The clean wing baseline flutter frequency is $\tilde{\omega}_f^o = 35.07$ (see Fig. 2, equivalent to $\omega_f = 22.4\,\text{rad}\,\text{s}^{-1}$ given in Table 2). It is shown with a vertical dashed line in Fig. 7. The damping ratio calculated by Eq. (40), illustrated with horizontal dashed lines in the figure, are respectively 0.134 and 0.061 for the masses tested. The optimal values of the couple $(\tilde{\omega}_{\text{T}}, \xi_{\text{T}})$ that provide the highest flutter speed are approximately $(31.94, 0.113)$ (to reach $\Upsilon_f/\Upsilon_f^o = 1.15$) and $(34.12, 0.048)$ (to reach $\Upsilon_f/\Upsilon_f^o = 1.06$) for the larger and smaller TMD mass respectively. The optimal frequency tuning therefore corresponds to a TMD frequency slightly below the clean wing flutter frequency. The *equal-peaks* technique for resonant systems (see [43]) also provides an expression to calculate an optimal frequency ratio between the primary and secondary structure. However, there is not much reason why it could apply in our *unstable* case. Overall, the optimal values found in our simulation are not far from the couple $(\tilde{\omega}_f^o, \xi_{\text{T}}^{*})$ and this is already a useful information.

The dependence of the flutter speed in ξ_{T} is not that sensible, except in the "danger zone" mentioned earlier, and is relatively smooth around ξ_{T}^{*}. On the other hand, there is an abrupt

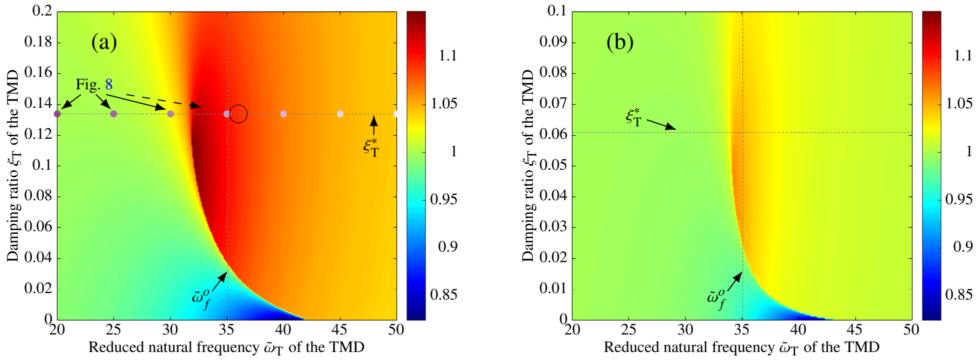

Figure 7: Critical flutter speed of the HALE wing as a function of the TMD properties (damping ration ξ_{T}, natural frequency $\tilde{\omega}_{\mathrm{T}}$) and for two different masses (a) $\tilde{m}_{\mathrm{T}} = 0.05$ and (b) $\tilde{m}_{\mathrm{T}} = 0.01$. The color map shows the normalized flutter speed (Υ_f/Υ^o_f). The complex eigenvalues associated with the purple markers in (a) are shown as a function of airspeed in Fig. 20. Horizontal and vertical dashed lines illustrate some particular values for the Den Hartog's optimal damping ξ^*_{T} and the clean wing flutter frequency $\tilde{\omega}^o_f$, respectively. The other absorber parameters are $\tilde{p} = 0.77$ and $\tilde{d} = 0$.

change in flutter speed around the optimum value when $\tilde{\omega}_{\mathrm{T}}$ varies. Even though the system studied here is slightly more complex than a 2D airfoil because flutter occurs with coupling involving the torsion mode and both the first and the second bending modes (see the mode shapes illustrated in Fig. 3(b)), a similar behaviour was found in previous studies on a 2D-airfoil with an attached TMD [44, 45]. Malher et al. [44] concluded that, for a more robust optimization purpose, it is safer to aim for a slightly larger value than the optimal $\tilde{\omega}_{\mathrm{T}}$-value. Further explanation on the discontinuous behavior in flutter speed can be explained by looking at Fig. 8. In the simulation presented in these figures, the mass ratio is $\tilde{m}_{\mathrm{T}} = 0.05$ and the damping ratio is equal to ξ^*_{T}. The curves shown correspond to the configurations plotted with dots in Fig. 7(a).

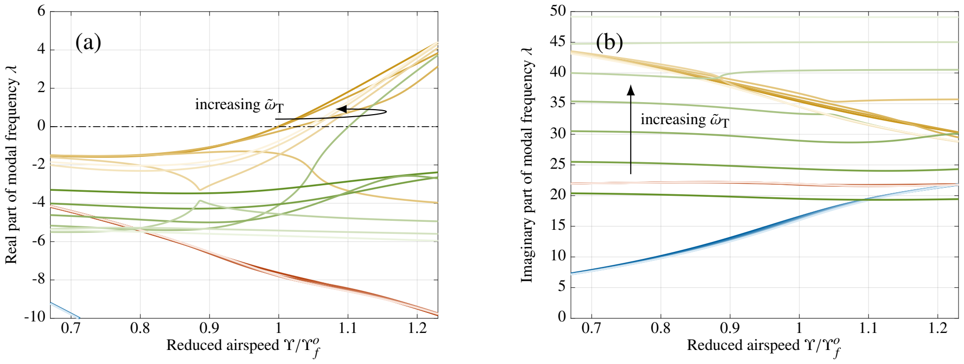

Figure 8: Real (a) and Imaginary (b) parts of the first four complex eigenvalues, as a function of the reduced airspeed Υ. The color scheme shows changes in the absorber tuning frequency $\tilde{\omega}_{\mathrm{T}}$, from $\tilde{\omega}_{\mathrm{T}} = 20$ in dark color to $\tilde{\omega}_{\mathrm{T}} = 50$ in light color. The corresponding flutter speed are depicted with purple dot markers in Fig. 7(a). Dimensionless spanwise and chordwise positions of the TMD are fixed at $\tilde{p} = 0.77$ and $\tilde{d} = 0$, respectively, and its mass ratio is $\tilde{m}_{\mathrm{A}} = 0.05$.

Figures 8(a) and (b) show, repectively, the real and imaginary parts of the first four natural complex eigenvalues as a function of the airspeed. At low airspeed, the blue, red and yellow curves can be associated with, in increasing frequency order, the first bending, the second bending and the torsional modes, respectively; the green curve directly relates to the TMD frequency – that is the one which is voluntarily varied in this study. When the speed increases, all modes get coupled and the denomination is not that clear but we will keep for the remaining of the paper the name *torsion mode*, *bending mode* and *TMD mode* to refer to the modes that are mainly of that kind at 0-airspeed, even though they are far from being purely torsion nor TMD motion when the airspeed increases. The first and second bending modes are not influenced much by the TMD presence. However, there is general trend that shows that the TMD strongly interacts with the torsion mode. At some point when the TMD frequency increases, its the TMD mode that become unstable while stabilizing the torsion mode, and allows to reach a value of $\Upsilon_f/\Upsilon_f^o \approx 1.1$ (see Fig. 8(a)). The TMD and torsion modes switched behavior after crossing (see Fig. 8(b)): the TMD natural frequency then decreases as the airspeed increases whereas the one of the torsion mode is almost constant.

These results are general for both mass ratio illustrated – a similar behaviour was actually found on the whole mass ratio range. They show that it is relevant to use the ξ_{T}^* value as damping parameter – because it is not sensible around this value, and a TMD frequency slightly above the clean wing flutter frequency – to avoid the abrupt drop that may occur below $\tilde{\omega}_f^o$. To be on the safe zone, $\tilde{\omega}_{\mathrm{T}} = 36$ will be used for the next analyses. The following section investigates in more details the effect ot the absorber mass and spanwise position. Investigation on the influence of the TMD chrodwise position will be performed in Section 4.1.2.

4.1.2. Influence of the TMD mass and spanwise position

In this section, the TMD frequency and damping ratio are fixed to the values $\tilde{\omega}_{\mathrm{T}} = 36$ and $\xi_{\mathrm{T}} = \xi_{\mathrm{T}}^*$, respectively. The position of the absorber chordwise is still $\tilde{d} = 0$ (i.e.attached to the wing elastic axis). With this configuration, the effect of both the TMD mass and its spanwise position on the critical flutter speed are investigated. The flutter speed simulated, as of function of both parameters, are illustrated in Fig. 9. It shows a relatively smooth behavior with the highest flutter speed obtained for the largest mass and spanwise position of approximately 3/4 of the span, towards the free end. The maximum value of $\Upsilon_f/\Upsilon_f^o = 1.09$ is reached for $\tilde{m}_{\mathrm{T}} = 0.05$ and $\tilde{p} = 0.734$. When either the TMD mass gets smaller or nearer to the clamped end, the flutter speed tends to that of a clean wing, because the TMD does not have any influence on the modes behavior any more.

For a given spanwise position $\tilde{p} = 0.77$, Fig. 10 shows the evolution of the complex eigenvalues as a function of the airspeed. As it was reported in [44], a larger TMD mass tends to stabilize the system and therefore postpone flutter. Indeed, with a larger mass comes a larger damping ratio (following the definition of ξ_{T}^*). The latter improves global stabilization and offers a higher critical airspeed. When the mass is high enough, the TMD mode is the one getting unstable instead of the torsion mode. Again, there is no pure TMD nor pure torsion mode but we refer to the modes that originate with mainly TMD and torsion modes à 0-airspeed.

A more original observation can be made on the influence of the TMD spanwise position. This is a parameter that is not usually studied in the literature because of the 2D-airfoil system usually employed. For a given mass, Fig. 9 shows an increase and then decrease in flutter speed when the TMD is moved towards the free end of the wing. This can be explained by the particular mode shape of the unstable mode at the flutter speed (see Fig. 3). One could have thought that placing the TMD at the free end will have the most influence on the flutter speed, but because the second bending mode is also involved in the overall dynamics, the global trend is not that simple. For a more thorough study on this aspect, one choses to fix the mass at its highest value

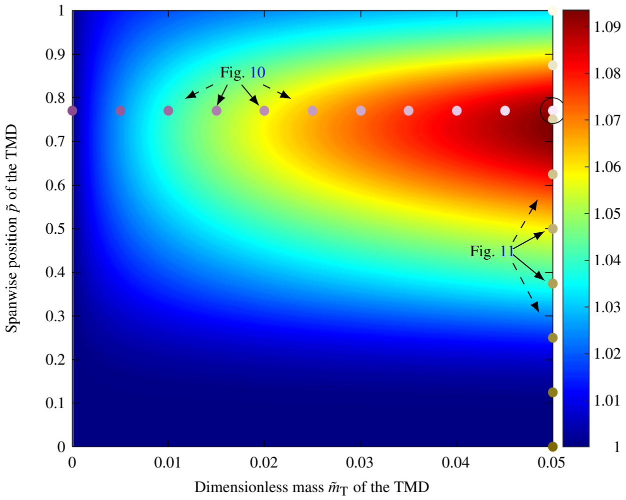

Figure 9: Critical flutter speed of the HALE wing as a function of the TMD spanwise stub position $\tilde{p}$ and mass $\tilde{m}_T$. The color map shows the normalized flutter speed $(\Upsilon_f/\Upsilon_f^o)$. The complex eigenvalues associated with the purple markers (horizontally placed) are shown as a function of airspeed in Fig. 10. The ones related to the brown dot markers (vertically placed) are shown as a function of airspeed in Fig 11. The other TMD parameters are $\tilde{\omega}_T = 36$, $\xi_T = \xi_T^*$, and $\tilde{d} = 0$.

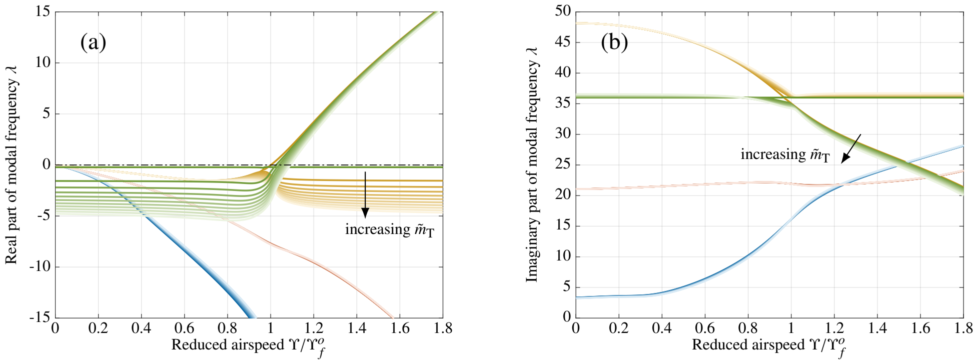

Figure 10: Real (a) and Imaginary (b) parts of the first four complex eigenvalues, as a function of the reduced airspeed Υ. The color scheme shows changes in the absorber mass $\tilde{m}_T$, from $\tilde{m}_T \approx 0$ in dark color to $\tilde{m}_T = 0.05$ in light color. The corresponding flutter speed are depicted with purple dot markers in Fig. 9. Dimensionless spanwise positions of the TMD is fixed at $\tilde{p} = 0.77$, its tuning frequency is $\tilde{\omega}_T = 36$, its damping is $\xi_T = \xi_T^*$ and its chordwise position is $\tilde{d} = 0$.

(i.e. $\tilde{m}_T = 0.05$) and plots the complex eigenvalue frequencies for different spanwise positions. This is illustrated in Fig. 11. In the second half of the wing span, the TMD and torsion modes seem to be strongly coupled and it is difficult to fully understand the phenomenon occurring.

Another representation is needed to get more usefull insights. As the TMD is, for now, attached on the wing centerline, it directly affects the bending motion (which, by aerodynamical coupling affects in turn the torsional motion). It is then interesting to see how the transverse displacement is affected by the presence of the TMD. For this matter, one fixes again the mass

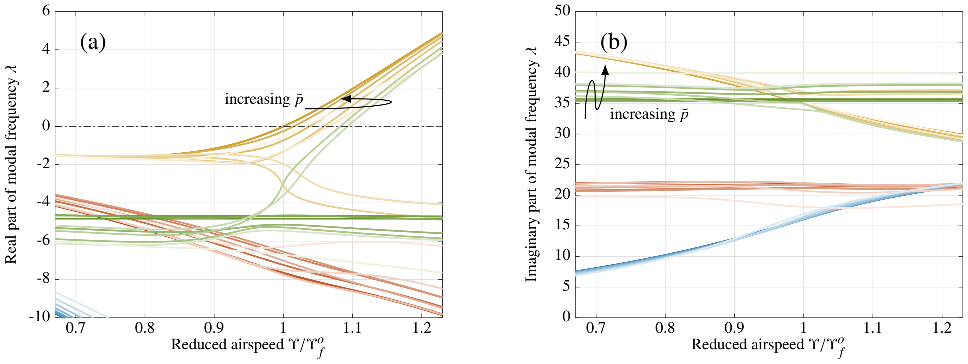

Figure 11: Real (a) and Imaginary (b) parts of the first four complex eigenvalues, as a function of the reduced airspeed Υ. The color scheme shows changes in the absorber spanwise position $\tilde{p}$, from $\tilde{p} = 0$ in dark color to $\tilde{p} = 1$ in light color. The corresponding flutter speed are depicted with brown dot markers in Fig. 9. The TMD mass is fixed at $\tilde{m}_{\mathrm{T}} = 0.05$, its tuning frequency is $\tilde{\omega}_{\mathrm{T}} = 36$, its damping is $\xi_{\mathrm{T}} = \xi_{\mathrm{T}}^*$ and its chordwise position is $\tilde{d} = 0$.

at $\tilde{m}_{\mathrm{T}} = 0.05$ and records, as a function of the TMD spanwise position, the position χ^* of the maximum transverse displacement over one cycle of vibration of the unstable mode at the flutter speed. This mathematically corresponds to:

$$\chi^* = \arg\max_{\chi}(\max_{\tau} |\upsilon_f(\chi, \tau)|)$$

where $\upsilon_f(\chi, \tau)$ is the time evolution of the mode shape of the unstable mode at the critical speed. Results of this analysis are illustrated in Fig. 12. Note that the position where the maximum value in torsion (ϕ) occurs is always at the tip (i.e. in $\chi = 1$) and do not gives useful information. There seems to be a correlation between the position of the absorber $\tilde{p}$, the position of the maximum displacement χ^* and the flutter speed reached. Indeed, the maximum in flutter speed – the flutter speed is also shown in Fig. 12 – is obtained when the absorber is located close to χ^*. The TMD most probably affects the most the dynamics in the zone of maximum amplitude of the primary structure.

Another interesting feature to quantify the TMD effectivness is looking at the energy dissipated by the damper, noted E_{dis}, over one cycle of vibration and as a function of the TMD position $\tilde{p}$. Recall this it is the only source of structural damping in the system. This energy is calculated with:

$$E_{\mathrm{dis}} = \int_0^{2\pi/\tilde{\omega}_f} \tilde{c}_{\mathrm{T}}(\dot{\upsilon}_f(\tilde{p}, \tau) - \dot{\delta}_f(\tau))^2 \,\mathrm{d}\tau$$

where $\tilde{\omega}_f$ and $\delta_f(\tau)$ are respectively the frequency and the TMD displacment of the unstable mode at the critical speed. This frequency corresponds to the imaginary part of the *purely* imaginary eigenvalue responsible for the onset of unstability. The energy dissipated is also illustrated in Fig. 12 and shows that it is directly related to the flutter speed as they both have the same trend. This can be explained by the fact that an efficient TMD that dissipates more energy will tend to stabilize the structure the most.

In order to see if any correlation could also be found with the effects of a TMD on a resonant system, one then looks at the phase difference, noted $\Delta\psi$, between the displacement at the

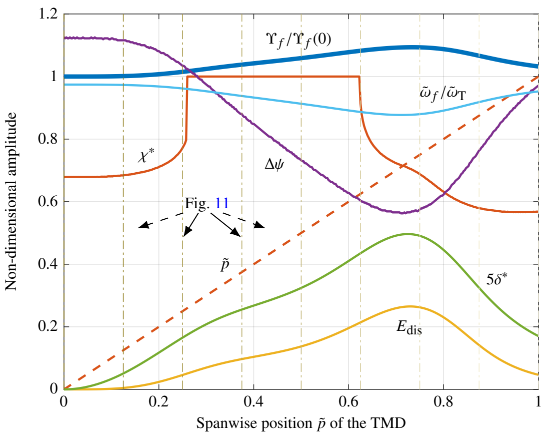

Figure 12: Evolution of different dimensionless metrics as a function of the spanwise position $\tilde{p}$ of the TMD. (—): energy dissipated E_{dis} by the absorber over one cycle of vibration of the unstable mode; (—) position χ^* of the maximum transverse displacement spanwise during one cycle of vibration of the unstable mode; (—) ratio of the flutter speed Υ_f over that of the clean wing Υ_f^o; (—) ratio of the frequency of the unstable mode $\tilde{\omega}_f$ over that of the TMD tuning $\tilde{\omega}_{\mathrm{T}}$; (—) maximum displacement of the TMD δ^* over one cycle of vibration of the unstable mode; (—) phase difference $\Delta\psi$ between the TMD movement and its attachment point on the main structure. The flutter speed related to the vertical dashed lines are depicted with brown dot markers in Fig. 9. The TMD mass is fixed at $\tilde{m}_{\mathrm{T}} = 0.05$, its tuning frequency is $\tilde{\omega}_{\mathrm{T}} = 36$, its damping is $\xi_{\mathrm{T}} = \xi_{\mathrm{T}}^*$ and its chordwise position is $\tilde{d} = 0$.

attachment point on the wing and the displacement of the TMD itself. It is defined looking at the time lag between the maximum values reached by each of them:

$$\Delta\psi = \left(\arg\max_{\tau} \left|\delta_f(\tau)\right| - \arg\max_{\tau} \left|v_f(\tilde{p},\tau)\right|\right)\tilde{\omega}_f$$

This phase difference $\Delta\psi$ is illustrated in Fig. 12. It is relatively small and its trend does not correspond to what have been guessed. Indeed, in a classical well set use of a TMD, the secondary structure moves out of phase at resonance with the primary one in order to dissipate maximum energy. With a phase lag evolving in the range in approximately 0.55 to 1.12, the absorber here acts more as an additional mass that affects mainly the wing natural frequencies. The effectivness of the TMD seems dominated by the increase in the TMD amplitude of movement and not by some phase optimisation. This is confirmed by looking at the value δ^*, also illustrated in Fig 12, that represents the maximum of δ over one cycle of vibration, as a function of the absorber position:

$$\delta^* = \max_{\tau} |\delta_f(\tau)|$$

The evolution of the flutter speed and the one of δ^* as a function of the absorber position shows a strong correlation and the maximum is reached in the same area.

Finally, the last parameter to investigate in order, again, to compare to the tuning of the TMD in a resonant system, is the value of the frequency $\tilde{\omega}_{\mathrm{T}}$ relatively to the frequency of the unstable mode $\tilde{\omega}_f$. Because the former is fixed in the simulation and the later evolves with the parameter $\tilde{p}$, the tuning between the primary and secondary structures evolves as well. The ratio in frequency $\tilde{\omega}_f/\tilde{\omega}_{\mathrm{T}}$ is plotted in Fig. 12. The largest differences are found in the 3/4-spanwise position zone, where the highest flutter speed occurs. It then seems that the perfect tuning of the TMD to the unstable frequency is not that important.

Overall, there are many parameters, all coupled to each other and it is tricky to give some accurate conclusions. The TMD damping ratio, frequency, and position on the wing all affect the system modal characteristics and therefore the occurrence of flutter.

4.1.3. Influence of the TMD chordwise positions

Finally, because flutter usually arises from the torsion mode destabilization, it is also relevant to study the influence of the chordwise position of the absorber. Indeed, when it is placed further from the beam elastic axis, it will influence more the torsional movment. Malher et al. [44] reported in their study on a 2D airfoil that the absorber should be placed at the leading edge. Note also that the aerodynamics model is different as we consider a unsteady approach. Anyway, as we have here under study a full wing, it is worth checking whether it is still the case whatever the spanwise position.

Because of its higher rigidity compared to the HALE wing, the Goland wing shows simpler dynamics with instability arising from coupling between the first bending and the first torsion mode (see Figs. 2(a) and 3(a)). We therefore start the analysis on this system. Figure 13 shows the evolution of the flutter speed of the Goland wing as a function of the absorber position on the wing, spanwise – parameter $\tilde{p}$, and chordwise – parameter $\tilde{d}$. The other fixed-value parmeters of the absorber are given in the caption of the figure. Recall that when $\tilde{d} - \tilde{a}$ varies from -1 to 1, the TMD position varies from the trailing edge to the leading edge of the wing. The clean Goland wing flutter speed is $\Upsilon_f^o = 1.60$ (equivalent to $U_f = 137.0\,\mathrm{m\,s^{-1}}$ given in Table 2).

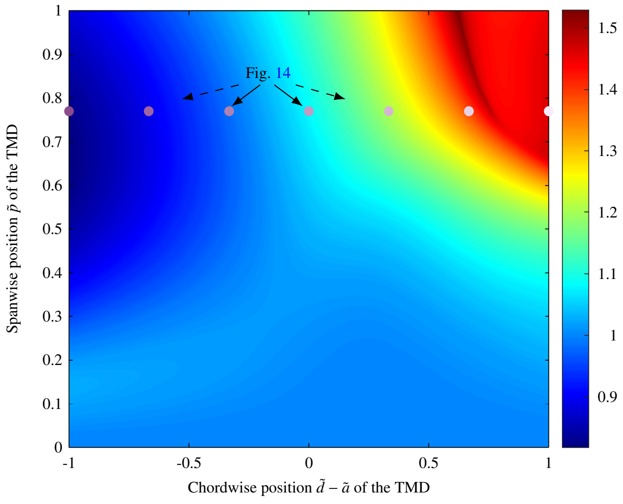

Figure 13: Critical flutter speed of the Goland wing as a function of the TMD spanwise stub position $\tilde{p}$ and chordwise $\tilde{d}$ positions. The color map shows the normalized flutter speed $(\Upsilon_f/\Upsilon_f^o)$. The complex eigenvalues associated with the purple markers are shown as a function of airspeed in Fig. 14. The other TMD parameters are $\tilde{m}_\mathrm{T} = 0.05$, $\tilde{\omega}_\mathrm{T} = 5$ (slightly higher than the clean Goland wing frequency), and $\xi_\mathrm{T} = \xi_\mathrm{T}^*$.

It can be observed on the figure that the higher flutter speed is obtained when the TMD is positioned towards the leading edge and towards the free end of the wing. The maximum value $\Upsilon_f/\Upsilon_f^o = 1.53$ is however not located at the furthest position but near the wing end at the parameters $(\tilde{d}-\tilde{a},\tilde{p}) = (0.625, 1)$. Anyway, this result is similar to what was observed by previous works, i.e. the absorber seems more efficient far from the elastic axis. However, it must be placed in front of the centreline, that is towards the leading edge, as it actually deteriorate the stability otherwise. Indeed for a fixed $\tilde{p}$, the flutter speed is lower when the TMD is placed behind the centreline, towards the trailing edge. It can even be worse than without absorber at all with a lowest flutter speed found equal to $\Upsilon_f/\Upsilon_f^o = 0.82$ at the point $(\tilde{d}-\tilde{a},\tilde{p}) = (-1, 0.67)$. The best area spanwise can be explained by the fact that the TMD should be place in higher vibration amplitude zone to fully play its stabilizing role, as it was discussed in Section 4.1.2.

For a fixed $\tilde{p}$-value of 0.77, the evolution of first three complex eigenvalues as a function of the airspeed are illustrated in Fig. 14. When the TMD is located towards the trailing edge, it destabilizes at a low airspeeds the torsion mode (red lines in Fig. 14) which shows a positive real part. Moving the TMD towards the leading edge changes the behaviour and makes, in turn, the bending mode (blue lines in Fig. 14) and the TMD mode (green lines in Fig. 14) go unstable at higher airspeed. Again, these mode nominations correspond to the natural frequencies of a purely uncoupled system at 0-airspeed. There is also a clear interaction between the modes, even at 0-airspeed because the TMD frequency $\tilde{\omega}_T$ is fixed to 5 but the corresponding modal frequency appears to be approximately 7 on Fig. 14.

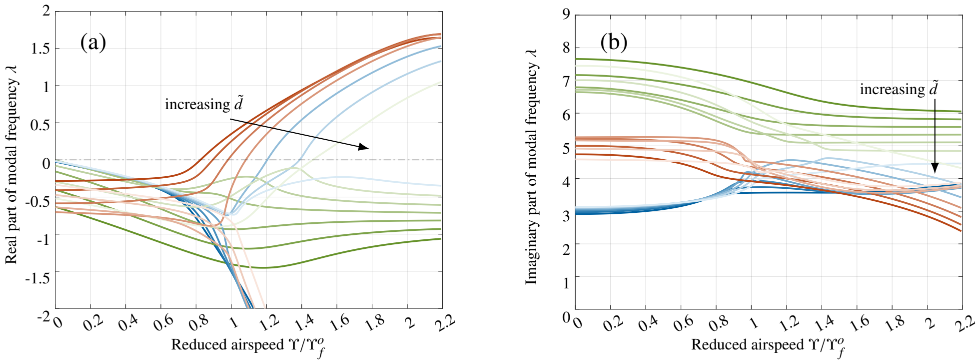

Figure 14: Real (a) and Imaginary (b) parts of the first four complex eigenvalues on the Goland wing, as a function of the reduced airspeed Υ. The color scheme shows changes in the absorber chordwise position $\tilde{d}$, from $\tilde{d} = \tilde{a} - 1$ (trailing edge) in dark color to $\tilde{d} = \tilde{a} + 1$ (leading edge) in light color. The corresponding flutter speed are depicted with purple dot markers in Fig. 13. The TMD mass is fixed at $\tilde{m}_T = 0.05$, its tuning frequency is $\tilde{\omega}_T = 5$, its damping is $\xi_T = \xi_T^*$ and its spanwise position is $\tilde{p} = 0.77$.

A similar analysis is now performed the HALE wing. Figure 15 shows the evolution of the flutter speed as a fonction of the TMD position spanwise and chordwise. The results are in this case much more complex and do not show any precise trend. There are some similarities with the Goland wing case (Fig. 13) with a decrease in flutter speed at some particular values spanwise and when the TMD is located at the trailing edge. It goes down to $\Upsilon_f/\Upsilon_f^o = 0.94$ for $(\tilde{d}-\tilde{a},\tilde{p}) = (-1, 0.73)$. The maximum in flutter speed $\Upsilon_f/\Upsilon_f^o = 1.20$ is reached on the leading edge at approximately the same spanwise position, for $(\tilde{d}-\tilde{a},\tilde{p}) = (1, 0.81)$.

There is however an area of low flutter speed at approximately 3/4 spanwise and 0.5 chordwise that is difficult to interpret. This difference in behaviour between the two wings simulated most probably come from the modes, and especifically the mode shapes, involved in the oc-

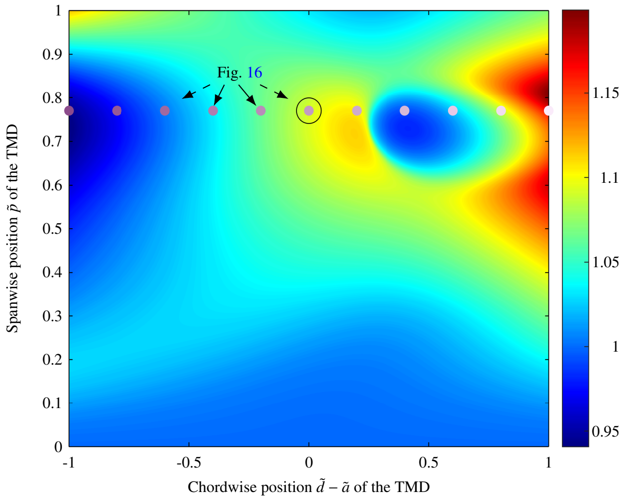

Figure 15: Critical flutter speed of the HALE wing as a function of the TMD spanwise stub position $\tilde{p}$ and chordwise $\tilde{d}$ positions. The color map shows the normalized flutter speed $(\Upsilon_f / \Upsilon_f^o)$. The complex eigenvalues associated with the purple markers are shown as a function of airspeed in Fig. 16. The other TMD parameters are $\tilde{m}_\mathrm{T} = 0.05$, $\tilde{\omega}_\mathrm{T} = 36$, and $\xi_\mathrm{T} = \xi_\mathrm{T}^*$

curence of the unstability. Because the second bending mode is also involved, the dynamics is more complex. Figure 16 shows the evolution of the complex eigenvalue as a function ot the airspeed for specific chordwise positions and at a fixed spanwise position $\tilde{p} = 0.77$ in order to investigate the variation in flutter speed observed. The modal characteristics seem relatively smooth with the TMD mode being first unstable and then the torsion mode (this corresponds to the color switch, from green to yellow in Fig. 16(a), of the mode whose real part gets positive). However, when this switch occurs, the flutter speed decreases. In other words, the flutter speed tends to increase with increasing $\tilde{d}$ except when it jumps back as the modes switch. It would be risky to try and interpret the results further because there are actually other dependent parameters, whom of which maybe most important is the tuning of the TMD frequency and damping, see the discussion of Section 4.1.2. These parameters are here fixed whereas the frequency of the unstable mode evolves with $\tilde{d}$.

Further investigation should be performed in order to have a general multi-input optimization in order to get the optimum setting. Some general trendlines can still be given by this study. The largest the attached mass the better regarding postponing flutter. This mass should be near a position of maximum displacement, which depends on the mode coupling involved at flutter, and towards the leading edge in order to have a direct effect on the torsional motion. Stiffness of the absorber should be carefully set because of the high sensitivity in frequency. Damping ratio seems less important and a value close to the Den Hartog's damping will most probably be a good choice.

4.2. Impact of the anechoic stub

The geometry of the stub depends on several parameters. In order to simplify a bit the analysis and study only general trends, some assumptions were made to relate the parameters

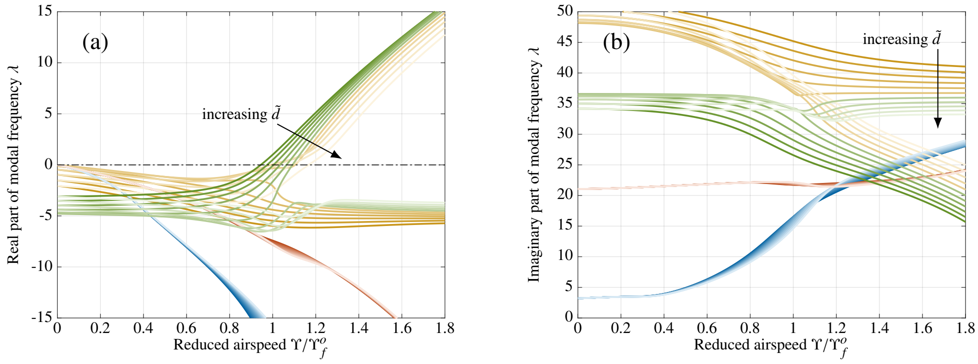

Figure 16: Real (a) and Imaginary (b) parts of the first four complex eigenvalues on the HALE wing, as a function of the reduced airspeed Υ. The color scheme shows changes in the absorber chordwise position $\tilde{d}$, from $\tilde{d} = \tilde{a} - 1$ (trailing edge) in dark color to $\tilde{d} = \tilde{a} + 1$ (leading edge) in light color. The corresponding flutter speed are depicted with purple dot markers in Fig. 15. The TMD mass is fixed at $\tilde{m}_{\mathrm{T}} = 0.05$, its tuning frequency is $\tilde{\omega}_{\mathrm{T}} = 36$, its damping is $\xi_{\mathrm{T}} = \xi_{\mathrm{T}}^*$ and its spanwise position is $\tilde{p} = 0.77$.

to each other. The stub is assumed to be a additional beam attached to the wing, modelled with the wave-based approach explained in Section 2. Its length is fixed in all simulations to be 10% of the chord length, i.e. $\tilde{l} = 0.1c/L$. The HALE wing design whose parameters are given in Table 1 is used as baseline system. The stub material properties are also fixed in all simulations to a density of $\rho_{\mathrm{A}} = 7850\,\mathrm{kg\,m^{-3}}$ and Young's modulus $E_{\mathrm{A}} = 210\,\mathrm{GPa}$. The beam cross section is assumed to be circular with radius R_{A}. All parameters are defined as a function of the imposed dimensionless mass $\tilde{m}_{\mathrm{A}}$ of the stub. Then, we get:

$$\sigma_l = \frac{E_{\mathrm{A}}\pi R_{\mathrm{A}}^2 L^2}{EI}, \quad \sigma_f = \frac{E_{\mathrm{A}}\pi R_{\mathrm{A}}^4}{4EI}, \quad \text{and} \quad \sigma_t = \frac{E_{\mathrm{A}}\pi R_{\mathrm{A}}^2 L^2}{GJ}, \quad \text{with} \quad R_{\mathrm{A}} = \sqrt{\frac{\tilde{m}_{\mathrm{A}} m}{\pi \tilde{l} \rho_{\mathrm{A}}}}$$

Overall, the radius and axial and flexural stiffnesses of the stub depend on the stub mass imposed.

4.2.1. *Influence of the reflection coefficient*

A critical parameter in the mitigation by an additional stub is the reflection coefficient $\tilde{r}$ used at the anechoic end. This coefficient should vary as a function of the frequency, as shown in [42]. However, to keep it simple and demonstrates the principle of such system to mitigate aeroelastic effects, one here use several specific values (similar to what was done in [40]). This section investigates the influence of both this coefficient and the spanwise position on the critical speed. The mass ratio of the stub is for now fixed to $\tilde{m}_{\mathrm{A}} = 0.001$. The stub is positionned on the wing centreline $\tilde{d} = 0$

Results from simulations are illustrated in Fig. 17. It shows the ratio of the critical flutter speed over that of the clean wing as a function of both parameters. At any given position spanwise, flutter is postpone when $\tilde{r}$ decreases. It means that the absorber is playing its role of damping vibration and stabilizing the whole system. Also for any given spanwise position, if the reflection coefficient is equal to 1, the stub acts as a simple attached small beam to the wing and do not have any effect. As the mass ratio is very small, it does not change neither the modal characteristics nor the critical speed ($\Upsilon_f/\Upsilon_f^o \approx 1$ when $\tilde{r} = 1$). The zone of particular interest is when the stub is positioned at approximately 3/4 of the span. In this area, it directly affects the modes and if $\tilde{r}$ is small enough, it can even make the occurrence of flutter completely disappear.

In order to numerically assess the curve in the $(\tilde{r}, \tilde{p})$-plane that gives the exact limit between the flutter and the no-flutter zone, one does it it several steps that are detailed next:

1. for a mesh grid in $\tilde{r}$ and $\tilde{p}$, predict the flutter speed with the same method as before, that is to use the method numbered 2 given in Section 2.3. Recall that the idea is to look for the two unknowns (λ_i, Υ) while imposing the real of the eigenvalue to be zero, solution of Eq. (22). As illustrated in Fig. 17, there may be some parameters-values for which this equation show no solution, i.e. there is no airspeed for which the real part of an eigenvalue becomes positive. Depending on the increments used in the mesh grid, this technique already gives an approximate solution for the limit curve.
2. In order to find the limit curve that separates the flutter and no-flutter zones, one chooses first to fix the parameter $\tilde{p}$. Then, an optimization problem is formulated to solve for the critical parameter $\tilde{r}^*$, which corresponds to the onset of the Hopf bifurcation. This is achieved by implementing a nested numerical procedure: for each iteration of a Newton-Raphson scheme on $\tilde{r}$, the maximum real part of the eigenvalues, λ_r, is computed over a predefined range of the airspeed Υ.
   Specifically, for each increment of $\bar{\Upsilon}$ of Υ, the system of equations $\mathrm{Re}(\det(\boldsymbol{A}(\lambda_r+\mathrm{i}\lambda_i, \bar{\Upsilon}))) = 0$ and $\mathrm{Im}(\det(\boldsymbol{A}(\lambda_r + \mathrm{i}\lambda_i, \bar{\Upsilon}))) = 0$ is solved to track the evolution of the eigenvalues. This corresponds to the methodology numbered 1 in Section 2.3. The objective is to identify $\tilde{r}^*$ such that the condition $\max_{\Upsilon}(\lambda_r) = 0$ is strictly satisfied. By iteratively repeating this process for various values of $\tilde{p}$, we successfully map the stability boundary in the $(\tilde{r}, \tilde{p})$-plane. This approach not only defines the transition to instability but also identifies the critical velocity Υ_f associated with each point on the flutter envelope.

The reason is somehow similar to what was explained in Section 4.1.2 on the TMD study: if the absorber is located at the position of maximum transverse displacement, it is where it has the more effects. This 3/4 zone was explained to come from coupling between the torsion mode and the first two bending modes. The physics involved are however different. The TMD consists of an extra mass that vibrates and can, under certain circumstance, capture energy from the primary structure; whereas the anechoic end of the stub directly impose some constraints on the displacement by restraining the amount of structural waves that are reflected.

Figure 18 shows the evolution of the first complex eigenvalues as a function of the $\tilde{r}$-reflection coefficient, for a given spanwise position chosen in the zone of interest ($\tilde{p} = 0.77$). At low airspeed, the stub affects almost only the first bending mode by reducing its natural frequency close to 0 and increasing quite dramatically the associated modal damping. It basically says that the stub constraints mainly the transverse displacement of the wing. This is normal because: it is now place on the wing elastic axis, and it is located at approximately the position of a node of vibration regarding the second bending mode. So the damping of neither the second bending mode nor the torsion mode is affected. As the airspeed increases, the behavior changes. The three modes get coupled because their frequency gets closer and as the torion mode is now involved, the stub affects its damping properties. As a consequence, as soon as the frequency of the torsion mode is influenced by the stub (at approximately $\Upsilon/\Upsilon_f^o \approx 0.6$), the associated damping significantly changes. When the three modes are directly in the same frequency range ($\Upsilon/\Upsilon_f^o > 1.2$) there is a really strong effect on the torsion modal damping which is completely stabilized. In this way, flutter disappears.

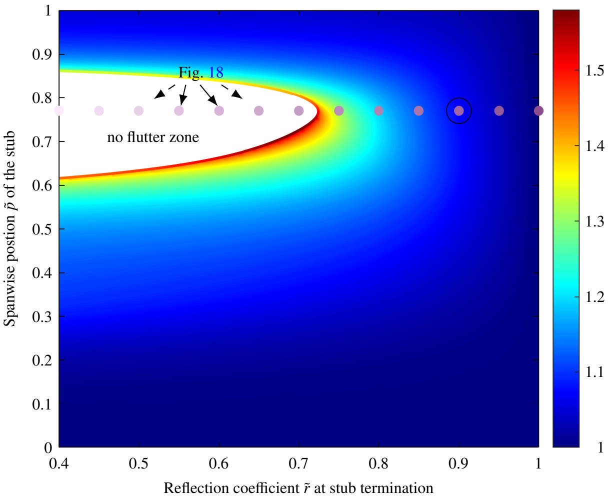

Figure 17: Critical flutter speed of the HALE wing as a function of the spanwise stub position $\tilde{p}$ and the reflection coefficient $\tilde{r}$ at the anechoic termination. The color map shows the normalized flutter speed (Υ_f/Υ_f^o). A no-flutter region is observed. The complex eigenvalues associated with the purple markers are shown in Fig. 18. The other stub parameters are $\tilde{m}_{\mathrm{A}} = 0.001$ and $\tilde{d} = 0$.

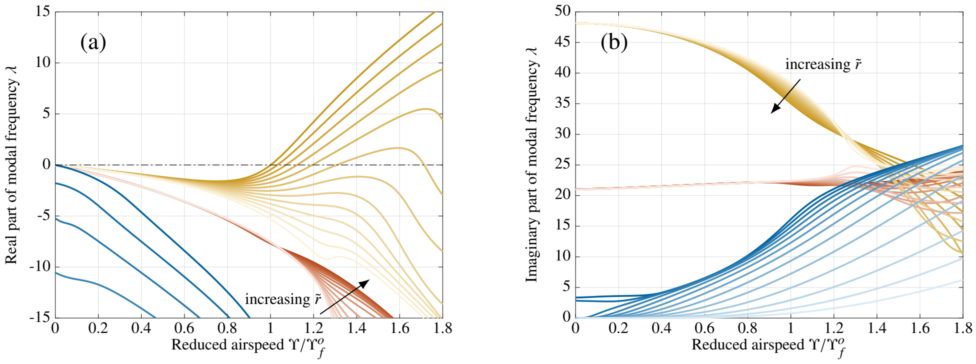

Figure 18: Real (a) and imaginary (b) parts of the first three complex eigenvalues versus the reduced airspeed Υ. The color map indicates variations in the stub reflection coefficient, ranging from $\tilde{r} = 0.4$ (light color) to $\tilde{r} = 1$ (dark colors). Corresponding flutter speeds are indicated by purple markers in Fig. 17. The other stub parameters are $\tilde{p} = 0.77$, $\tilde{d} = 0$, and $\tilde{m}_{\mathrm{A}} = 0.001$.

At other $\tilde{p}$ spanwise positions, the displacement of the wing is relatively naturally smaller and therefore the restraint brought by the stub presence has got less influence. For instance at the wing end ($\tilde{p} = 1$) the maximum value obtained for the flutter speed is solely $\Upsilon_f/\Upsilon_f^o \approx 1.05$ for the smallest $\tilde{r}$-value simulated. This mean that even a very efficient anechoic end can have only small effect on the flutter speed if not placed correctly spanwise. Understanding the mode shapes involved at or near critical speed is essential to predict the relative effectinvess of the device.

4.2.2. Influence of the stub mass and stiffness properties

Because of the assumption made on designing the stub, mass and stiffness brought by the added beam are directly related. Indeed an heavier stub, knowing that material properties and length are fixed, means a thicker element and therefore a stiffer one. As a consequence both effects are studied simultaneously.

Results on the flutter speed, as a function of the stub mass and spanwise position, are illustrated in Fig. 19. In these simulations the stub is still attached to the wing elastic axis ($\tilde{d} = 0$) and the reflection coefficient is $\tilde{r} = 0.9$. For $\tilde{p} = 0.77$, the first complex eigenvalues are plotted as function ot the airspeed in Fig. 20. The results are really similar to what was presented in the previous Section 4.2.1 when changing the reflection coefficient. The system behaves in a similar way when $\tilde{m}_{\mathrm{A}}$ increases as when $\tilde{r}$ decreases. Indeed, 1. a 0-mass is approximatively equivalent to a coefficient of $\tilde{r} = 1$, i.e. there is no effect on flutter; 2. at a given $\tilde{p}$-position, flutter speed is always postponed for heavier (and then stiffer) stub, which was similar as saying that any $\tilde{r}$-value is always benefitial on the critical speed; and 3. there is a zone around 3/4 spanwise where the effect of the stub is more marked.

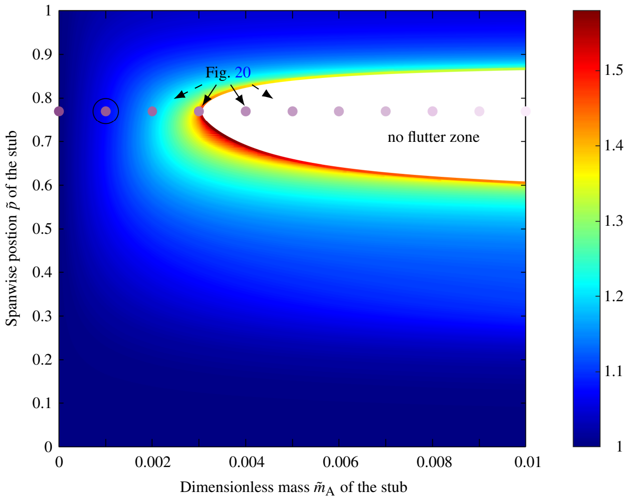

Figure 19: Critical flutter speed of the HALE wing as a function of the spanwise stub position $\tilde{p}$ and mass $\tilde{m}_{\mathrm{A}}$. The color map shows the normalized flutter speed $(\Upsilon_f/\Upsilon_f^o)$. A no-flutter region is observed. The complex eigenvalues associated with the purple markers are shown in Fig. 20. The other stub parameters are $\tilde{d} = 0$ and $\tilde{r} = 0.9$.

The reason of this third observation is similar as before. Looking at Fig. 20, one sees that a small stub affects only the first bending mode at low airspeed by almost completely annihilating it: almost 0 frequency and very high damping (the real part of the associated eigenvalues goes quickly smaller than -10). However when the airspeed increases and coupling between modes occur from aerodynamics effects, the stub will start to affect the damping of the torsion mode and even stabilize it completly to remove flutter. It is interesting to compare these results with the use of a TMD. It the latter case, when the mass was increased, they were, at some point, a transfer between the torsion mode and the TMD mode, such that the TMD mode would become unstable even though the torsion mode was more damped (see Fig. 10). The behaviour observed with the stub differs, as the quasi-anechoic termination only introduces artificial damping and does not

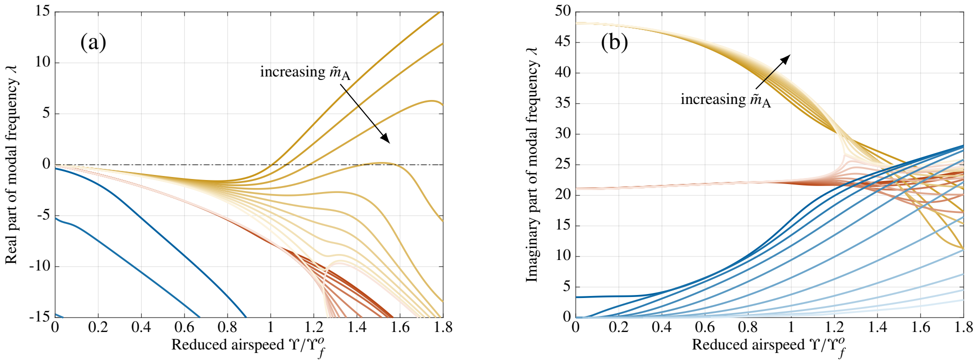

Figure 20: Real (a) and imaginary (b) parts of the first three complex eigenvalues versus the reduced airspeed Υ. The color map indicates variations in the stub mass, ranging from $\tilde{m}_A \approx 0$ (dark color) to $\tilde{m}_A = 0.01$ (light color). Corresponding flutter speeds are indicated by purple markers in Fig. 19. The other stub parameters are $\tilde{p} = 0.77$, $\tilde{d} = 0$, and $\tilde{r} = 0.9$.

involve a secondary structure capable of independent oscillation. The improvement observed at approximately the 3/4 spanwise location arises from the coupling between the torsional mode and the second bending mode.

5. Conclusion

This paper presented a wave-based framework for the aeroelastic flutter analysis of flexible wings, providing an exact formulation that naturally accounts for wave reflection and transmission without relying on modal truncation or spatial discretization. The proposed approach was successfully validated against benchmark cases, such as the Goland and HALE wings, accurately predicting flutter and divergence speeds across various aerodynamic models, including quasi-static and unsteady formulations. The study investigated two passive control strategies for flutter mitigation:

- Tuned-Mass-Damper: While effective at postponing flutter, the TMD's performance is highly sensitive to its tuning frequency, mass ratio, and spanwise positioning. It was shown that a TMD is most effective when placed in areas of maximum vibration amplitude (approximately 3/4 spanwise for the cases tested) and towards the wing's leading edge to directly influence torsional motion.

- Anechoic Stub: This device proved to be a more efficient and robust damping technique than the TMD. Unlike tuned devices, the anechoic stub acts directly on wave propagation and provides broadband attenuation. Strategic positioning of the stub—specifically around the 3/4 spanwise location—can significantly increase the flutter speed or even cause the instability to disappear entirely by suppressing the wave mechanisms responsible for resonance build-up.

Despite these promising results, several difficulties and areas for future research were identified. The wave-based approach results in a nonlinear transcendental eigenvalue problem. While simple cases allow for analytical dispersion relations, more complex governing equations may require numerically expensive evaluations. Tracking the lowest eigenvalues as airspeed increases does not guarantee that a higher-frequency mode will not become unstable first. Robust frameworks for solving non-polynomial nonlinear eigenvalue problems are required for more complex systems. While the theoretical benefits are clear, the practical feasibility of achieving an anechoic stub with high reflection coefficients (e.g., $r = 0.9$) at low frequencies in axial vibration requires further experimental investigation.

In conclusion, the wave-based framework provides a powerful alternative to traditional modal methods for flutter prediction and highlights the anechoic stub as a superior passive control mechanism for enhancing the aeroelastic stability of slender wings

Appendix A. Dispersion relation

Substituting a general wave-form solution ($\boldsymbol{u}(\chi,\tau) = \hat{\boldsymbol{u}}\mathrm{e}^{\kappa\chi}\mathrm{e}^{\lambda\tau} + \mathrm{c.c}$) in the governing equation of motion (9), and solving for arbitrary τ and χ, yield two linear homogeneous algebraic equations in the unknown coefficients $\hat{\upsilon}$ and $\hat{\phi}$. Those can be written in the following matrix form:

$$\boldsymbol{D}(\kappa,\lambda,\Upsilon)\hat{\boldsymbol{u}} = \begin{bmatrix} D_{11} & D_{12} \\ D_{21} & D_{22} \end{bmatrix} \begin{bmatrix} \hat{\phi} \\ \hat{\upsilon} \end{bmatrix} = \boldsymbol{0}. \tag{A.1}$$

The analytical expression of the elements of the $\boldsymbol{D}$-matrix depends on the aerodynamic model used. Quasi-steady and unsteady aerodynamics cases are detailed next.

Appendix A.1. Quasi-steady aerodynamics

In a simple quasi-steady aerodynamic model, without added-mass effects, see [5, 25, 46], the lift and moment are defined as:

$$F_w = 2\pi\rho U b\left[-\dot{w} + U\phi + b\left(\frac{1}{2} - \tilde{a}\right)\dot{\phi}\right] \tag{A.2a}$$

$$M_\phi = b\left(\frac{1}{2} + \tilde{a}\right)F_w - \frac{1}{2}\pi\rho U b^3\dot{\phi}. \tag{A.2b}$$

Following the parametrization given in Section 2.1, the dimensionless version of Eq. (A.2) becomes:

$$\tilde{F}_\upsilon = 2\pi\mu\Upsilon\left[-\dot{\upsilon} + \Upsilon\phi + \tilde{b}\left(\frac{1}{2} - \tilde{a}\right)\dot{\phi}\right] \tag{A.3a}$$

$$\tilde{M}_\phi = \tilde{b}\left(\frac{1}{2} + \tilde{a}\right)\tilde{F}_w - \frac{1}{2}\pi\mu\Upsilon\tilde{b}^2\dot{\phi}. \tag{A.3b}$$

The components of the $\boldsymbol{D}$-matrix, such as defined in Eq. (A.1), are:

$$D_{11} = -\gamma\kappa^2 + \beta\lambda^2 + 2\pi\mu\Upsilon\tilde{a}^2\tilde{b}^2\lambda - \pi\mu\Upsilon^2\tilde{b}(1 + 2\tilde{a}) \tag{A.4a}$$

$$D_{12} = -\tilde{e}\lambda^2 + \pi\mu\Upsilon\tilde{b}(1 + 2\tilde{a})\lambda \tag{A.4b}$$

$$D_{21} = -\tilde{e}\lambda^2 + \pi\mu\Upsilon\tilde{b}(2\tilde{a} - 1)\lambda - 2\pi\mu\Upsilon^2 \tag{A.4c}$$

$$D_{22} = \kappa^4 + \lambda^2 + 2\pi\mu\Upsilon\lambda. \tag{A.4d}$$

As mentioned in Section 2.2, solving for the non-trivial solution of Eq. (A.1) gives three complex roots in κ^2 that can be found analytically. Therefore, for any given complex frequency λ, there are six complex roots $\pm\kappa_i(\lambda)$ $(i = 1,\ 2,\ 3)$. Only three of which are kept, following the sign rule detailed in Section 2.2 and the expression (15).

In a general configuration, the coupling between $\hat{\upsilon}$ and $\hat{\phi}$ wave amplitudes is defined via the coefficients:

$$\begin{aligned}
\bar{X}_1(\lambda) &= -\frac{D_{11}(\kappa_1(\lambda))}{D_{12}(\kappa_1(\lambda))} = -\frac{-\gamma\kappa_1(\lambda)^2 + \beta\lambda^2 + 2\pi\mu\Upsilon\tilde{a}^2\tilde{b}^2\lambda - \pi\mu\Upsilon^2\tilde{b}(1+2\tilde{a})}{-\tilde{e}\lambda^2 + \pi\mu\Upsilon\tilde{b}(1+2\tilde{a})\lambda} \\
X_i(\lambda) &= -\frac{D_{22}(\kappa_i(\lambda))}{D_{21}(\kappa_i(\lambda))} = -\frac{\kappa_i(\lambda)^4 + \lambda^2 + 2\pi\mu\Upsilon\lambda}{-\tilde{e}\lambda^2 + \pi\mu\Upsilon\tilde{b}(2\tilde{a}-1)\lambda - 2\pi\mu\Upsilon^2} \quad \text{for } i = \{2,3\}
\end{aligned}$$

Even though theoretically, from Eq. (A.1), one has $X_i = 1/\bar{X}_i$ $(i = 1, 2, 3)$, the formulations given in Section 2.2 only use the coefficients $\bar{X}_1$, X_2 and X_3 defined above. The reason is that they are the ones which tend to 0 when bending-torsion coupling becomes negligible, that is if both $\Upsilon \to 0$ (i.e. no aerodynamic forces) and $\tilde{e} = 0$ (i.e. no inertia coupling). In this configuration, the $\boldsymbol{D}$-matrix is diagonal; meaning there is no torsion-bending coupling. Note that the wavenumbers solution of the dispersion relation are then those of classical torsional and bending waves.

If one is interested in a quasi-steady model equivalent to a "degenerate unsteady model" that accounts for all non-circulatory terms but disregards any feedback from the wake's inflow [5, 47], then simply takes $C_k = 1$ in the more general expression (A.5) given in the next section.

Appendix A.2. Unsteady aerodynamics

The previous section showed how to obtained the dispersion relation on a simple quasi-steady model. Using the unsteady Theodorsen model given in Section 2.1, the reasoning to get the wavenumbers and the coupling coefficients is the same, only the expressions are slightly more complicated. In this case, the components of the $\boldsymbol{D}$-matrix, in the dimensionless form, are:

$$\begin{aligned}
D_{11} &= -\gamma\kappa^2 + \left(\beta + \pi\mu\tilde{b}^3\left(\frac{1}{8} + \tilde{a}^2\right)\right)\lambda^2 + \ldots \\
&\qquad \pi\mu\Upsilon\tilde{b}^2\left(\frac{1}{2} - \tilde{a} + C_k\left(2\tilde{a}^2 - \frac{1}{2}\right)\right)\lambda - \pi\mu\Upsilon^2\tilde{b}C_k(1+2\tilde{a}) && \text{(A.5a)} \\
D_{12} &= \left(-\tilde{e} + \pi\mu\tilde{a}\tilde{b}^2\right)\lambda^2 + \pi\mu\Upsilon\tilde{b}C_k(1+2\tilde{a})\lambda && \text{(A.5b)} \\
D_{21} &= \left(-\tilde{e} + \pi\mu\tilde{a}\tilde{b}^2\right)\lambda^2 - \pi\mu\Upsilon\tilde{b}\left(1 + C_k(1-2\tilde{a})\right)\lambda - 2\pi\mu\Upsilon^2 C_k && \text{(A.5c)} \\
D_{22} &= \kappa^4 + \left(1 + \pi\mu\tilde{b}\right)\lambda^2 + 2\pi\mu\Upsilon C_k\lambda, && \text{(A.5d)}
\end{aligned}$$

with $C_k = C(\omega_r)$ the Theodorsen's circulation function of the reduced frequency ω_r. In classical aeroelasticity problems, see for instance [2], the assumed harmonic motion is usually defined with a complex exponential coefficient $\mathrm{e}^{\mathrm{i}\omega t}$, where ω is the vibrating (real) frequency, giving the expression $\omega_r = b\omega/U$ for the reduced frequency. With the particular formalism used in (11) that considers a time-dependency coefficient in $\mathrm{e}^{\lambda\tau}$, the reduced frequency ω_r to use in the Theodorsen function becomes $\omega_r = -\mathrm{i}\tilde{b}\lambda/\Upsilon$.

The coupling coefficients are calculated in the same way as in the quasi-static case, keeping only $\bar{X}_1$, X_2 and X_3.

References

[1] Mayuresh J Patil and Dewey H Hodges. Flight dynamics of highly flexible flying wings. *Journal of Aircraft*, 43(6):1790–1799, 2006.

[2] Dewey H. Hodges and G. Alvin Pierce. *Introduction to Structural Dynamics and Aeroelasticity*. Cambridge Aerospace Series. Cambridge University Press, 2 edition, 2011.

[3] D.H. Hodges and E.H. Dowell. Nonlinear equations of motion for the elastic bending and torsion of twisted nonuniform rotor blades. Technical report, NASA-TN-D-7818, NASA communication, 1974.

[4] Martin Goland. The flutter of a uniform cantilever wing. *Journal of Applied Mechanics*, 12(4):A197–A208, 03 1945.

[5] Marco Berci. On aerodynamic models for flutter analysis: A systematic overview and comparative assessment. *Applied Mechanics*, 2(3), 2021.

[6] B. R. Mace. Wave reflection and transmission in beams. *Journal of Sound and Vibration*, 97:237–246, 1984.

[7] B. Chouvion, C. H. J. Fox, S. McWilliam, and A. A. Popov. In-plane free vibration analysis of combined ring-beam structural systems by wave propagation. *Journal of Sound and Vibration*, 329:5087–5104, 2010.

[8] CM Wu and B Lundberg. Reflection and transmission of the energy of harmonic elastic waves in a bent bar. *Journal of Sound and Vibration*, 190(4):645–659, 1996.

[9] L. Cremer, M. Heckl, and E. E. Ungar. *Structure-Borne sound*. Springer-Verlag, Munich, 1988.

[10] K. F. Graff. *Wave motion in Elastic Solids*. Ohio State University Press, 1975.

[11] Sebastian Liska and Earl H Dowell. Continuum aeroelastic model for a folding-wing configuration. *AIAA Journal*, 47(10):2350–2358, 2009.

[12] Nidish Narayanaa Balaji, Matthew RW Brake, and Michael J Leamy. Wave-based analysis of jointed elastic bars: Nonlinear periodic response. *Nonlinear Dynamics*, 110(3):2005–2031, 2022.

[13] Nidish Narayanaa Balaji, Matthew RW Brake, and Michael J Leamy. Wave-based analysis of jointed elastic bars: stability of nonlinear solutions. *Nonlinear Dynamics*, 111(3):1971–1986, 2023.

[14] Stefan Guttel, Roel Van Beeumen, Karl Meerbergen, and Wim Michiels. Nleigs: A class of fully rational krylov methods for nonlinear eigenvalue problems. *SIAM Journal on Scientific Computing*, 36(6):A2842–A2864, 2014.

[15] Pieter Lietaert, Karl Meerbergen, Javier Pérez, and Bart Vandereycken. Automatic rational approximation and linearization of nonlinear eigenvalue problems. *IMA Journal of Numerical Analysis*, 42(2):1087–1115, 2022.

[16] Mohammed Kassem, Zhichun Yang, Yingsong Gu, Wei Wang, and Ehab Safwat. Active dynamic vibration absorber for flutter suppression. *Journal of Sound and Vibration*, 469:115110, 2020.

[17] Jihad E AlQasimi, Sultan M Ghazzawi, and Rayeh N Al-Dala'ien. Multi-mass tuned mass damper for enhanced passive control of aircraft wing vibration. In *Smart Materials, Adaptive Structures and Intelligent Systems*, volume 89275, page V001T03A003. American Society of Mechanical Engineers, 2025.

[18] Edouard Verstraelen, Giuseppe Habib, Gaetan Kerschen, and Grigorios Dimitriadis. Experimental passive flutter suppression using a linear tuned vibration absorber. *AIAA Journal*, 55(5):1707–1722, 2017.

[19] SNY Gerges, R Jordan, FA Thieme, JL Bento Coelho, and JP Arenas. Muffler modeling by transfer matrix method and experimental verification. *Journal of the Brazilian Society of Mechanical Sciences and Engineering*, 27(2):132–140, 2005.

[20] M.J. Brennan. Control of flexural waves on a beam using a tunable vibration neutraliser. *Journal of Sound and Vibration*, 222(3):389–407, 1999.

[21] Adrien Pelat, François Gautier, Stephen C Conlon, and Fabio Semperlotti. The acoustic black hole: A review of theory and applications. *Journal of Sound and Vibration*, 476:115316, 2020.

[22] Cameron A. McCormick and Micah R. Shepherd. Design optimization and performance comparison of three styles of one-dimensional acoustic black hole vibration absorbers. *Journal of Sound and Vibration*, 470:115164, 2020.

[23] R. Alcorta, B. Chouvion, G. Michon, and O. Montagnier. On the use of frictional dampers for flutter mitigation of a highly flexible wing. *International Journal of Non-Linear Mechanics*, 156:104515, 2023.

[24] Rafic M Ajaj and Michael I Friswell. Aeroelasticity of compliant span morphing wings. *Smart materials and structures*, 27(10):105052, 2018.

[25] H. Haddadpour and R.D. Firouz-Abadi. Evaluation of quasi-steady aerodynamic modeling for flutter prediction of aircraft wings in incompressible flow. *Thin-Walled Structures*, 44(9):931–936, 2006.

[26] AH Nayfeh, BK Hammad, and MR Hajj. Discretization effects on flutter aspects and control of wing/store configurations. *Journal of Vibration and Control*, 18(7):1043–1055, 2012.

[27] B. Chouvion, A. A. Popov, S. McWilliam, and C. H. J. Fox. Vibration modelling of complex waveguide structures. *Computers and Structures*, 89:1253–1263, 2011.

[28] B. Chouvion. Vibration analysis of beam structures with localized nonlinearities by a wave approach. *Journal of Sound and Vibration*, 439:344–361, 2019.

[29] DJ Mead. Waves and modes in finite beams: application of the phase-closure principle. *Journal of Sound and Vibration*, 171(5):695–702, 1994.

[30] E.L. Allgower and K. Georg. *Introduction to numerical continuation methods*. Springer-Verlag, 2003.

[31] Arion Pons and Stefanie Gutschmidt. Aeroelastic flutter of continuous systems: A generalized laplace transform method. *Journal of Applied Mechanics*, 83(8):081005, 2016.

[32] Arion Pons. Pseudospectral continuation for aeroelastic stability analysis. *Journal of Vibration and Acoustics*, 144(4):044501, 2022.

[33] Timo Betcke, Nicholas J Higham, Volker Mehrmann, Christian Schröder, and Françoise Tisseur. Nlevp: A collection of nonlinear eigenvalue problems. *ACM Transactions on Mathematical Software (TOMS)*, 39(2):1–28, 2013.

[34] Stefan Güttel and Françoise Tisseur. The nonlinear eigenvalue problem. *Acta Numerica*, 26:1–94, 2017.

[35] M. J. Patil. *Nonlinear Aeroelastic Analysis, Flight Dynamics,and Control of a Complete Aircraft*. PhD thesis, Georgia Institute of Technology, 1999.

[36] Joseba Murua, Rafael Palacios, and J. Michael R. Graham. Assessment of wake-tail interference effects on the dynamics of flexible aircraft. *AIAA Journal*, 50(7):1575–1585, 2012.

[37] Rafic M. Ajaj, Farag K. Omar, Tariq T. Darabseh, and Jonathan Cooper. Flutter of telescopic span morphing wings. *International Journal of Structural Stability and Dynamics*, 19(06):1950061, 2019.

[38] Flávio Luiz Cardoso Ribeiro, Pedro Paglione, Roberto Gil Annes da Silva, and Marcelo Santiago de Sousa. Aeroflex: a toolbox for studying the flight dynamics of highly flexible airplanes. Sao Luis, Brasil, 2012. 7th International Congress of Mechanical Engineering, CONEM.

[39] B. Chouvion. A wave approach to show the existence of detached resonant curves in the frequency response of a beam with an attached nonlinear energy sink. *Mechanics Research Communications*, 95:16–22, 2019.

[40] Hangyuan Lv and Michael J Leamy. Damping frame vibrations using anechoic stubs: analysis using an exact wave-based approach. *Journal of Vibration and Acoustics*, 143(5):051012, 2021.

[41] C Mei. In-plane vibrations of classical planar frame structures—an exact wave-based analytical solution. *Journal of Vibration and control*, 16(9):1265–1285, 2010.

[42] Vivien Denis, François Gautier, Adrien Pelat, and J Poittevin. Measurement and modelling of the reflection coefficient of an acoustic black hole termination. *Journal of Sound and Vibration*, 349:67–79, 2015.

[43] G. Habib, T. Detroux, R. Viguié, and G. Kerschen. Nonlinear generalization of Den Hartog's equal-peak method. *Mechanical Systems and Signal Processing*, 52-53:17–28, 2015.

[44] Arnaud Malher, Cyril Touzé, Olivier Doaré, Giuseppe Habib, and Gaëtan Kerschen. Flutter Control of a Two-Degrees-of-Freedom Airfoil Using a Nonlinear Tuned Vibration Absorber. *Journal of Computational and Nonlinear Dynamics*, 12(5):051016, 2017.

[45] K. Dhital and B Chouvion. Passive aeroelastic control of a near-ground airfoil with a nonlinear vibration absorber. *Aerospace*, 11:1043, 2024.

[46] Y. C. Fung. *An introduction to the theory of aeroelasticity*. Dover Publications, 2008.

[47] Raymond L Bisplinghoff, Holt Ashley, and Robert L Halfman. *Aeroelasticity*. Addison-Wesley Publishing Company, Cambridge, MA, 1955.